Cooperative Cobinding of Synthetic and Natural Ligands to the Nuclear Receptor PPARγ

Jinsai Shang [1], Richard Brust [1], Sarah A. Mosure [1,2,3], Jared Bass [1], Paola Munoz-Tello [1], Hua Lin [4], Travis S. Hughes [5,6], Miru Tang [7], Qingfeng Ge [7], Theodore M. Kamenecka [4], and Douglas J. Kojetin [1,4,*]

[1] Department of Integrative Structural and Computational Biology, The Scripps Research Institute, Jupiter, Florida 33458, USA
[2] Summer Undergraduate Research Fellows (SURF) program, The Scripps Research Institute, Jupiter, Florida 33458, USA
[3] Skaggs Graduate School of Chemical and Biological Sciences, The Scripps Research Institute, Jupiter, Florida 33458, USA
[4] Department of Molecular Medicine, The Scripps Research Institute, Jupiter, Florida 33458, USA
[5] Center for Biomolecular Structure and Dynamics, The University of Montana, Missoula, Montana 59812, USA
[6] Department of Biomedical and Pharmaceutical Sciences, The University of Montana, Missoula, Montana 59812, USA
[7] Department of Chemistry and Biochemistry, Southern Illinois University, Carbondale, Illinois 62901, USA

*Correspondence should be addressed to D.J.K. (e-mail: dkojetin@scripps.edu)

Crystal structures of peroxisome proliferator-activated receptor gamma (PPARγ) have revealed overlapping binding modes for synthetic and natural/endogenous ligands, indicating competition for the orthosteric pocket. Here we show that cobinding of a synthetic ligand to the orthosteric pocket can push natural and endogenous PPARγ ligands (fatty acids) out of the orthosteric pocket towards an alternate ligand-binding site near the functionally important omega (Ω) loop. X-ray crystallography, NMR spectroscopy, all-atom molecular dynamics simulations, and mutagenesis coupled to quantitative functional assays reveal that synthetic ligand and fatty acid cobinding can form a "ligand link" to the Ω loop and synergistically affect the structure and function of PPARγ. These findings contribute to a growing body of evidence indicating ligand binding to nuclear receptors can be more complex than the classical one-for-one orthosteric exchange of a natural or endogenous ligand with a synthetic ligand.

INTRODUCTION

Thiazolidinediones (TZDs), also called glitazones, are synthetic agonists of the peroxisome proliferator-activated receptor gamma (PPARγ) nuclear receptor with potent anti-diabetic efficacy in patients with type 2 diabetes (1). TZDs were initially discovered in phenotypic screens as compounds with anti-diabetic efficacy (2), and later studies identified PPARγ as the molecular target (3). After an increase in clinical use of TZD drugs such as rosiglitazone (*Avandia*) in the early 2000s, the use of TZDs in diabetic patients has dropped significantly due to adverse side effects, including bone loss and water retention. These observations have spawned efforts to determine the molecular mechanisms by which TZDs and other synthetic PPARγ ligands exert beneficial antidiabetic effects and adverse effects.

Crystal structures of the PPARγ ligand-binding domain (LBD) have been critical in determining the molecular mechanism of action of PPARγ-binding ligands. Overall, the structure of the PPARγ LBD is described as a three-layer helical sandwich fold composed of 12 α-helices containing a dynamic or flexible internal ligand-binding pocket. The PPARγ ligand-binding pocket (**Figure 1A**) is among the largest in the nuclear receptor superfamily (4), ranging from 1200–1400 Å^3 in crystal structures with three branches described as "T" or "Y" shaped (5). Branch I is located proximal to helix 12, which forms a critical part of the activation function-2 (AF-2) coregulator binding surface; branch II is located near the β-sheet surface, close to the predicted ligand entry/exit site where helix 3 meets helix 6 and the helix 11/12 loop; and branch III is also located near the β-sheet surface but deeper in the pocket near helix 5 (6-8). One of the first crystal structures of PPARγ was solved bound to the synthetic TZD ligand rosiglitazone (9), which revealed critical details on the molecular contacts formed between a ligand and the binding pocket of the receptor. Subsequent crystal structures of PPARγ bound to dietary medium-chain fatty acids (MCFAs) and long-chain unsaturated fatty acids (UFAs), the latter of which are endogenous PPARγ ligands (10), revealed overlapping binding modes with synthetic ligands that occupy all three branches of the orthosteric pocket (5, 11-15). These crystal structures and others, combined with biochemical ligand displacement assays (16-19), revealed that synthetic and natural ligands compete for binding to the same orthosteric pocket.

However, recent studies have shown that synthetic PPARγ ligands that were originally designed to bind to the orthosteric pocket can also bind to an alternate site (20-25). The alternate site that partially overlaps with

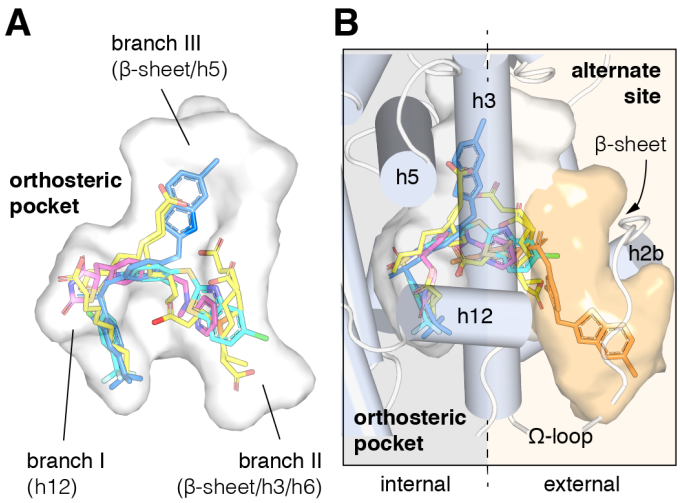

Figure 1. Structural locations of PPARγ orthosteric pocket and alternate site. (**A**) The T/Y-shaped orthosteric pocket can accommodate one or more natural ligands such as nonanoic acid (C9; yellow sticks; PDB: 4EM9) and synthetic ligands such as rosiglitazone (pink sticks; PDB: 4EMA) or T2384 (light and dark blue sticks representing different crystallized binding modes; PDB: 3K8S, chain A and B, respectively). (**B**) The orthosteric pocket (white pocket surface) is completely enclosed within the alpha helical sandwich fold of the ligand-binding domain (LBD). Ligands such as T2384 (orange sticks; PDB: 3K8S, chain B) can also bind to a solvent accessible alternate site (orange pocket surface) distinct from the orthosteric pocket, structurally defined as the region between helix 3 (h3) and the flexible Ω-loop (dotted line separating the region internal to the LBD, grey background; and external to the LBD, light orange background).

one of the arms of the T/Y-shaped orthosteric pocket near the β-sheet surface (branch II), but it uniquely occupies space in a solvent exposed pocket formed by the flexible omega (Ω)-loop that precedes helix 3 (**Figure 1B**). Structural studies have linked ligand occupancy of branch I (i.e., the helix 12 subpocket) within the orthosteric pocket to robust stabilization of the AF-2 surface, increased "classical" transcriptional activation, and side effects associated with TZDs in part driven by hydrogen bonds formed between the TZD head group and residues within branch I (26). In contrast, ligands that either do not form hydrogen bonds in the helix 12/branch I subpocket, or bind to a combination of branch II and the alternate site, can stabilize the Ω-loop region and a nearby loop. Stabilization of this region near the Ω-loop can inhibit phosphorylation of a serine residue (S273 in PPARγ isoform 1 or S245 in isoform 2) by the Cdk5 kinase and is associated with anti-diabetic efficacy (24, 25, 27, 28).

We were initially interested in the structural changes that allows the TZD edaglitazone (29, 30) to fit within the branch I/helix 12 subpocket. Edaglitazone contains a bulky benzo[b]thiophene group adjacent to the TZD head group, in contrast to other TZD-bound PPARγ crystal structures, which have smaller moieties (e.g., phenyl) adjacent to the TZD head group. We solved the crystal structure of the PPARγ LBD bound to edaglitazone at the orthosteric pocket, which unexpectedly revealed a bacterial MCFA cobound to the alternate site. MCFAs are not only present in bacteria; they are also dietary mammalian natural PPARγ ligands obtained from foods such as oils and dairy products (31) that display high serum concentrations (μM–mM) and activate PPARγ transcription, regulate the expression of PPARγ target genes, and influence cellular differentiation, adipogenesis, and insulin sensitization in mice (15, 32, 33). The cobound MCFA provides a "ligand link" to the flexible Ω-loop, and crystal structures of PPARγ bound to covalent orthosteric antagonists revealed that synthetic ligands extensions within the orthosteric pocket can push fatty acid cobinding modes towards the Ω-loop. Inspired by these findings, we solved several crystal structures showing that endogenous UFAs can be pushed from their orthosteric binding modes to an alternate site cobinding mode when a synthetic TZD ligand binds to the orthosteric pocket. Using NMR spectroscopy, molecular dynamics simulations, isothermal titration calorimetry (ITC), and mutagenesis coupled to functional assays, we show that cobinding of a synthetic ligand and fatty acid affects the conformation of the AF-2 surface, synergistically enhances coactivator interaction, and may affect PPARγ transcription in cells.

RESULTS

Edaglitazone is a TZD PPARγ agonist

Edaglitazone is similar in chemical structure to a commonly used PPARγ agonist rosiglitazone (**Figure 2A**), both of which possess the prototypical TZD head group. Edaglitazone has a bulkier 5-methyl-2-phenyloxazole tail group compared to the N-methylpyridin-2-amine tail group in rosiglitazone. Furthermore, there is a substitution of the phenyl moiety adjacent to the TZD head group in rosiglitazone for a bulkier benzo[b]thiophene moiety in edaglitazone. Edaglitazone and rosiglitazone display similar affinities for PPARγ, 141 nM and 93 nM respectively, in a fluorescent tracer ligand displacement assay (**Figure 2B**). The compounds also show similar potencies in a TR-FRET biochemical assay on increasing the interaction of a peptide derived from the TRAP220 coactivator (**Figure 2C**; 132 nM and 186 nM respectively) and decreasing the interaction with a peptide derived from the NCoR corepressor (**Figure 2D**; 171 nM and 432 nM respectively); as well as in a cell-based transcriptional reporter assay (**Figure 2E**; 5.4 nM and 3.2 nM respectively).

Crystal structure of PPARγ cobound to edaglitazone and a MCFA

We obtained crystals of the PPARγ ligand-binding domain (LBD) by co-crystallizing protein incubated with edaglitazone. Crystals formed in the I4 space group, a different space group compared to the >150 crystal structures of PPARγ deposited in the PDB. The structure was solved at 2.1 Å (**Supplementary Table 1**) as a homodimer with two molecules in the asymmetric unit

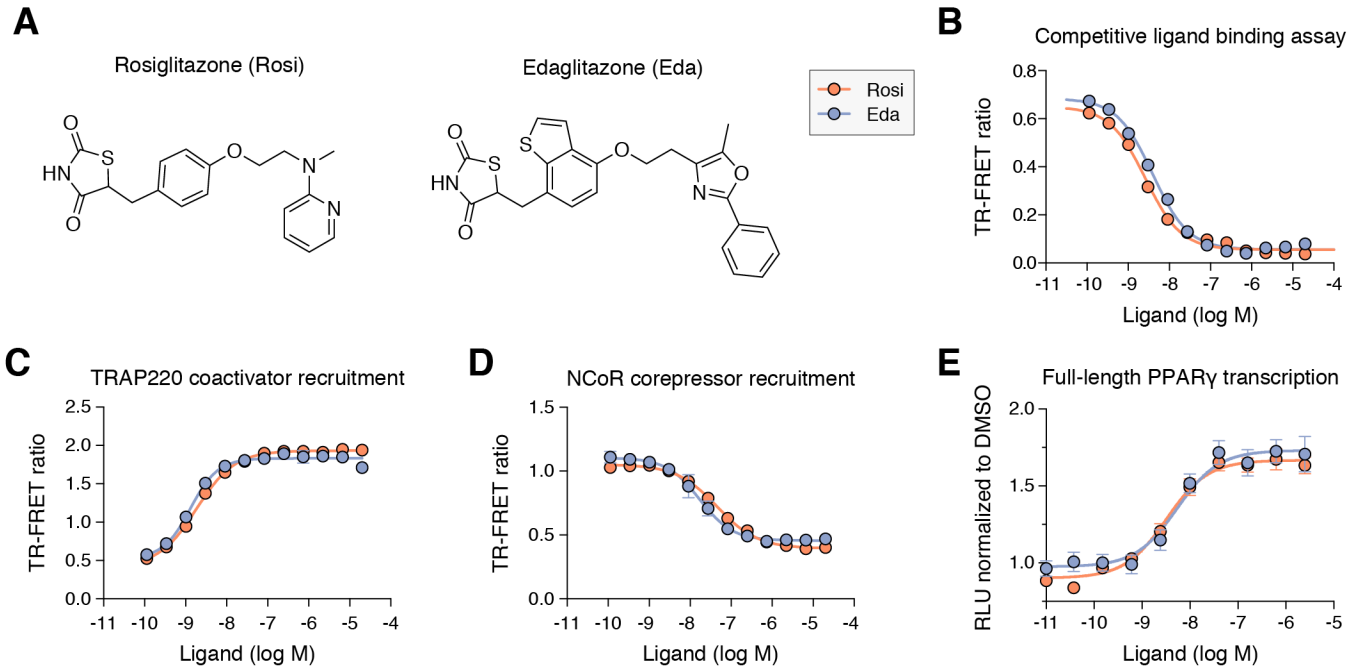

Figure 2. Edaglitazone is a thiazolidinedione (TZD) PPARγ agonist related to rosiglitazone. (**A**) Chemical structures of edaglitazone and rosiglitazone. (**B**) TR-FRET ligand displacement assay. Data plotted as the average and S.D. of three experimental replicates. (**C,D**) TR-FRET coregulator interaction assay data in the presence of peptides derived from (**C**) TRAP220 coactivator and (**D**) NCoR corepressor. Data plotted as the average and S.D. of three experimental replicates. (**E**) Cell-based luciferase reporter assay measuring full-length PPARγ transcription in HEK293T cells; RLU = relative luciferase units. Data plotted as the average and S.E.M. of four experimental replicates.

(chains A and B) as an alpha helical sandwich fold. In the absence of a coregulator peptide, helix 12 typically adopts two distinct conformations in chains A and B in previously solved crystal structures—an "active" conformation, where helix 12 is docked into the AF-2 surface; and an atypical conformation via contacts to another symmetry related molecule within the unit cell. However, in our edaglitazone-bound structure, both chains adopt an active helix 12 conformation (**Figure 3A**) with nearly identical backbone conformations (Cα r.m.s.d. 0.186 Å).

Strong electron density was observed for three ligands in both chain A and B molecules (**Figure 3B; Supplementary Figure 1**): one edaglitazone bound to the canonical or orthosteric pocket; a second edaglitazone to a surface pocket created through an interaction between two symmetry-related protein molecules (**Supplementary Figure 2**); and a MCFA consistent with the size of a nonanoic acid (C9) molecule bound to a solvent accessible region near helix 3, the β-sheet surface of the orthosteric pocket, and the flexible Ω-loop region. Notably, a previous study showed that PPARγ expressed in *E. coli* can retain MCFAs from the bacteria, predominately C9, which function as natural PPARγ agonists (15, 32). The combined binding of the C9 and the second edaglitazone may have contributed to the stability of the PPARγ Ω-loop, which is often characterized with very poor or absent electron density in most published crystal structures.

When bound to the orthosteric pocket, rosiglitazone (**Figure 3C**) and edaglitazone (**Figure 3D**) make conserved hydrogen bonds via the TZD head group to the side chains of S289 (helix 3), H323 (helix 5), H449 (helix 10/11), and Y473 (helix 12). The TZD head group of rosiglitazone also makes a hydrogen bond to Q286 (helix 3), which is not present in the edaglitazone-bound structure due to a 2.8 Å shift of the Q286 side chain from the rosiglitazone-bound position (5.7 Å away from the TZD 2-carbonyl position). This occurs due to a rearrangement of the N-terminal region of helix 3 in the edaglitazone-bound structure, which affects the conformation of Q286 more than S289 (**Figure 3E**). Additional conformational changes in the edaglitazone-bound structure move helix 6 and the loop connecting helix 6–7 away from the ligand-binding pocket, and the movement of helix 3 also causes a concomitant movement of helix 12. Finally, F363 and M364 are found in the loop connecting helix 6–7 with secondary structure elements classified as a hydrogen bonded turn and bend, respectively according to DSSP analysis (34). These residues undergo a shift of 6.0 Å (Phe363) and 2.6 Å (M364) away from the ligand-binding pocket to accommodate the benzo[b]thiophene in the edaglitazone-bound structure, along with several other subtler changes (< 1 Å) that accommodate 5-methyl-2-phenyloxazole tail group near the β-sheet (**Figure 3F**).

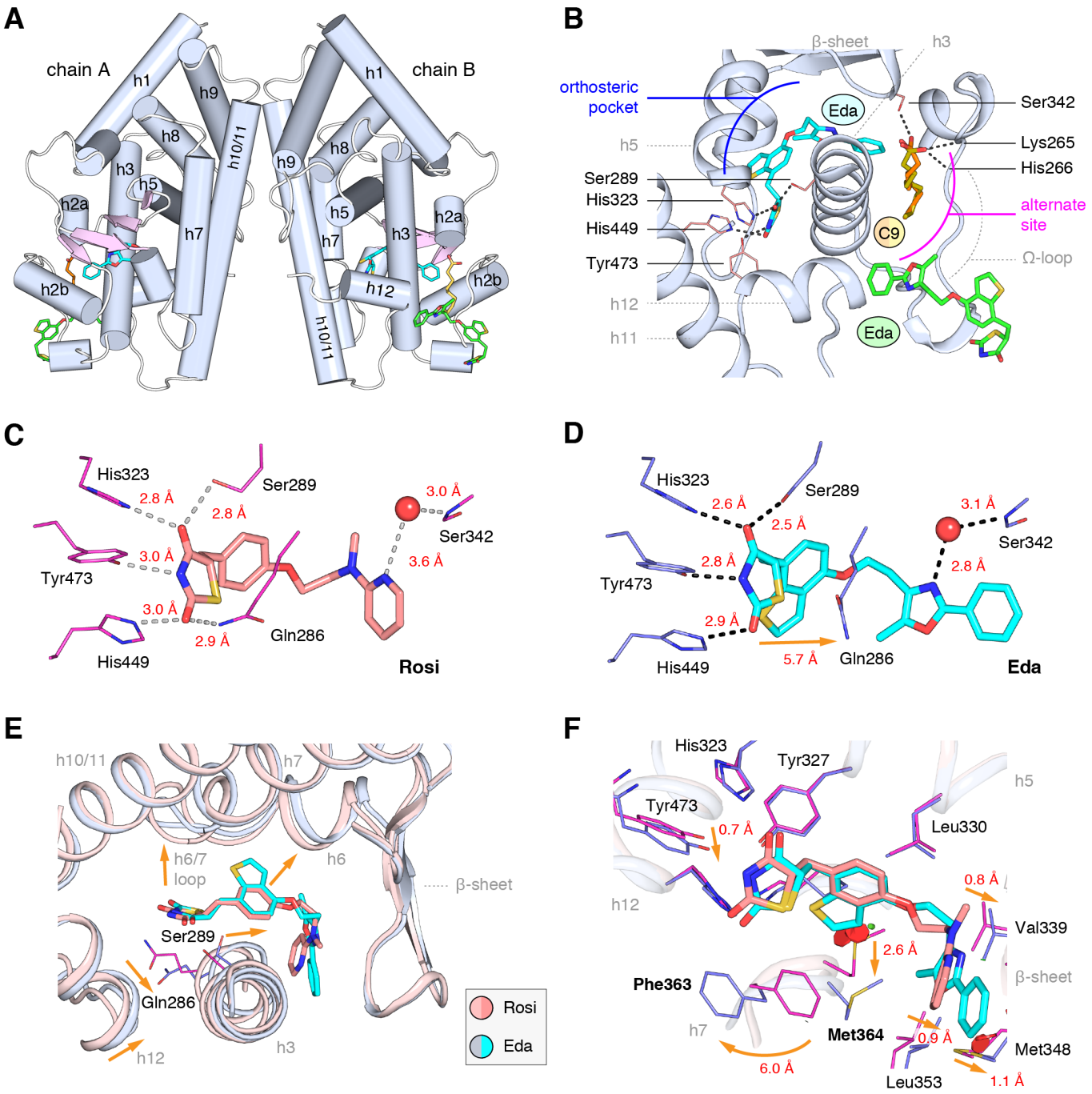

Figure 3. Co-crystal structure of edaglitazone-bound PPARγ LBD reveals a cobound bacterial MCFA. (**A**) Overall structure (helices, light blue; strands, pink) with two bound edaglitazone (EDA) ligands, one to the canonical orthosteric pocket (blue) and another to a surface pocket (green), and a C9 ligand bound to an alternate site (yellow and orange in chain A and B, respectively). (**B**) Molecular interactions between PPARγ and the EDA and C9 ligands. Dotted lines denote hydrogen bonds. (**C,D**) Comparison of the hydrogen bond interactions between PPARγ and (**C**) rosiglitazone (PDB: 2PRG) and (**D**) edaglitazone. Dotted lines denote hydrogen bonds. (**E,F**) Conformational changes relative to rosiglitazone-bound PPARγ (PDB: 2PRG) that allow the orthosteric pocket to adapt to binding the bulkier benzo[b]thiophene moiety in edaglitazone. The changes (orange arrows) include (**E**) shifting of the backbone of helix 3, helix 6, helix 6/7 loop, and helix 12; and (**F**) large movements of the Phe363 and M364 side chains adjacent to the benzo[b]thiophene moiety.

MCFAs cobound in other PPARγ crystal structures bound to synthetic ligands

A previous study reported a crystal structure of PPARγ LBD that was obtained using protein purified from *E. coli*, which revealed the presence of bound endogenous bacterial MCFAs (32). Specifically, three molecules of C9 were observed in the orthosteric pocket (**Figure 4A**) overlapping in space where edaglitazone is bound in our structure (**Figure 4B**). In our edaglitazone-bound crystal structure, there is clear density for a bacterial MCFA near helix 3, the β-sheet surface of the orthosteric pocket, and the flexible Ω-loop region. This region is referred to as an "alternate" or "allosteric" site,

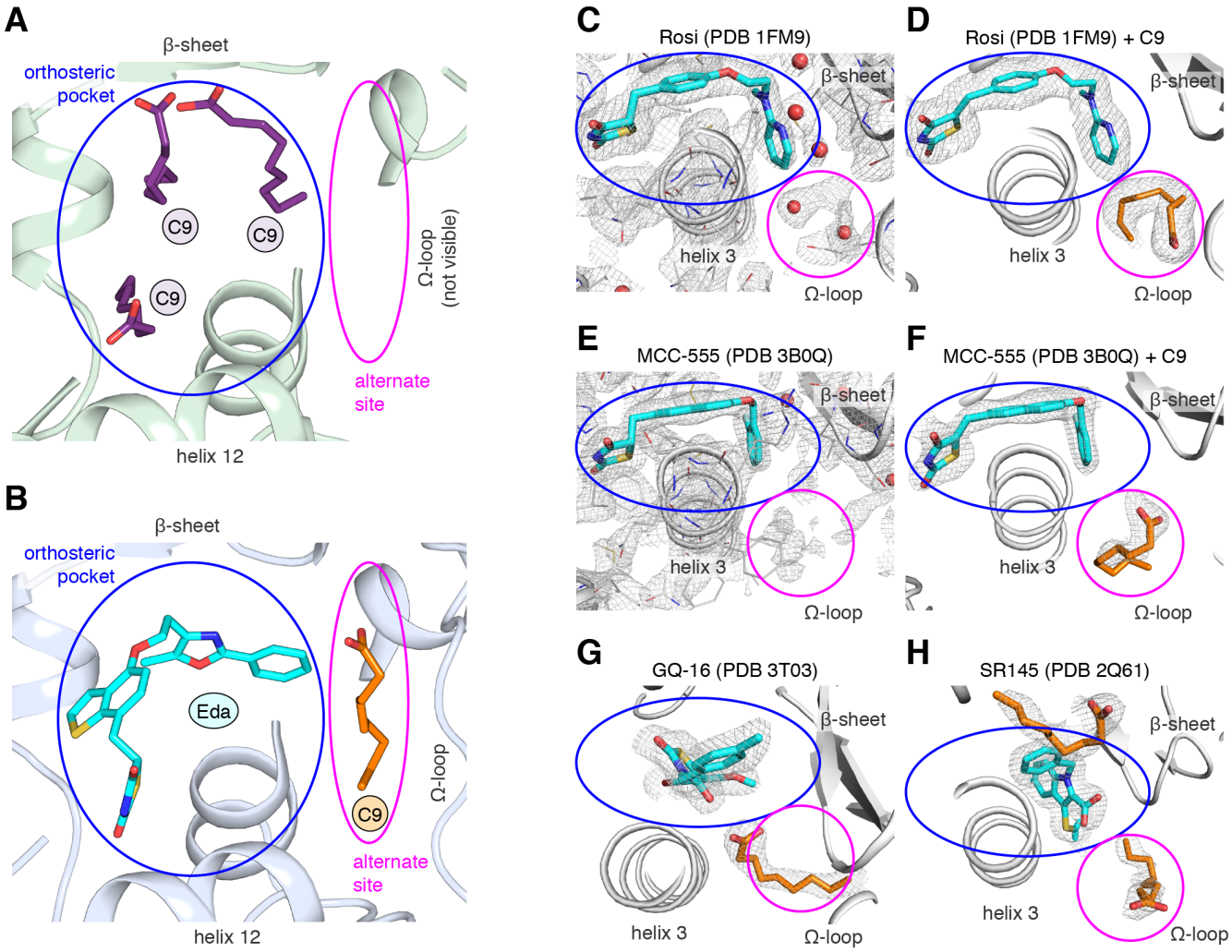

Figure 4. MCFA electron density in previously solved synthetic ligand-bound PPARγ LBD crystal structures. (**A,B**) Comparison of a crystal structure of PPARγ LBD with (**A**) three molecule of C9 bound to the orthosteric pocket (PDB: 4EM9) and (**B**) C9 bound to the alternate site with edaglitazone bound to the orthosteric pocket. (**C-F**) Electron density maps for previously determined TZD-bound (blue) crystal structures shown with (**C,E**) original deposited structural models and (**D,F**) C9 (orange) modeled and refined into density present in the alternate site. (**G,H**) C9 (orange) modeled and refined into previously determined crystal structures of PPARγ bound to (**G**) GQ-16 (blue) and (**H**) SR145 (blue). Omit maps ($2F_O–F_C$) contoured at 1 σ in all but the C9 modeled into the GQ-16 structure, which was contoured at 0.5 σ. The orthosteric pocket and alternate site are circled in blue and magenta, respectively.

because other studies have shown that synthetic ligands that have crystallized in the orthosteric pocket can also bind to this alternate site. Alternate site binding occurs via a second molar equivalent of ligand, i.e. one bound to the orthosteric pocket and a second to the alternate site (20-22); when the orthosteric pocket is blocked by a covalent antagonist inhibitor that physically blocks the orthosteric pocket (20, 22, 24, 25); or one equivalent through an alternate binding mode (24, 25).

We wondered whether there could be density present for a bacterial MCFA in previously published crystal structures of PPARγ bound to synthetic ligands, which may not have been modeled during structure determination because it could have been unexpected at the time. Analysis of the electron density maps deposited to the PDB for two relatively high resolution (~2 Å) crystal structures bound to rosiglitazone (PDB: 1FM6) and MCC-555 (PDB: 3B0Q) revealed extra unidentified densities suggesting there could be a MCFA bound in a similar manner to what we observed in the edaglitazone structure. In a crystal structure of RXRα-PPARγ LBD heterodimer where PPARγ was bound to rosiglitazone (PDB: 1FM6) solved to 2.1 Å (35), two water molecules were modeled next to rosiglitazone where the C9 is bound in our edaglitazone structure (**Figure 4C**). We found that replacement of the water molecules with a C9 better describes the density in this region (**Figure 4D**). In a crystal structure of PPARγ bound to MCC-555 (PDB: 3B0Q) solved to 2.1 Å, we also found unmodeled density (**Figure 4E**) consistent with a MCFA present in the same region (**Figure 4F**). Additionally, we found density consistent with a MCFA in crystal structures of PPARγ bound to GQ-16 (**Figure 4G**) and SR145 (**Figure 4H**), which had been solved to 2.1 Å and 2.2 Å, respectively (36, 37). These observations suggest that cobound bacterial MCFAs may be present in other synthetic ligand-bound PPARγ crystal structures. Impor-

tantly, MCFAs are also dietary natural ligands present in oils and dairy products consumed by mammals; thus, the fortuitous discovery that bacterial MCFAs can cobind with synthetic orthosteric ligands has structural and functional relevance to PPARγ.

NMR validates cobinding of C9 with a TZD bound to the orthosteric pocket

To determine the degree to which bacterial MCFAs are bound to PPARγ, we performed differential 2D [^{1}H, ^{15}N]-TROSY HSQC NMR analysis of ^{15}N-labeled PPARγ LBD subjected to a delipidation protocol and "native" protein that was not subjected to delipidation (**Supplementary Figure 3**), which revealed subtle chemical shift and peak intensity/line broadening changes. Notably, titration of C9 (**Supplementary Figure 4**) into native PPARγ caused additional selective NMR chemical shift changes, indicating that native protein is likely only partially bound to (i.e., is not saturated with) bacterial MCFAs. We have observed that, compared to delipidated proteins, native NMR chemical shift changes are batch dependent. Native PPARγ NMR spectra can also appear nearly identical to delipidated PPARγ NMR spectra, indicating that the amount of bacterial lipid that may be bound and retained during purification can vary from substoichiometric to almost none. These changes can result from how the protein purification is performed, such as the length of chromatography or dialysis steps, or variability of fatty acid content depending on the bacterial growth media used, as the use of minimal vs. rich media can change exogenous fatty acid content within bacteria (38).

We also performed differential NMR analysis of rosiglitazone-bound forms of native and delipidated PPARγ to determine if there could be cobinding of a synthetic TZD to native protein bound to a substoichiometric amount of a bacterial MCFA. Although the NMR spectra overlay very closely (**Supplementary Figure 5**), subtle NMR chemical shift perturbations were observed for a select number of peaks (**Figure 5A**), including residues in our crystal structure near the C9 bound to the alternate site on helix 3 (V277, Q283, and G284), as well as residues within the AF-2 surface on helix 5 (L317 and K319) and helix 12 (L465, I472, and K474). Furthermore, several NMR peaks with weak intensities in the native form showed narrower, more in-

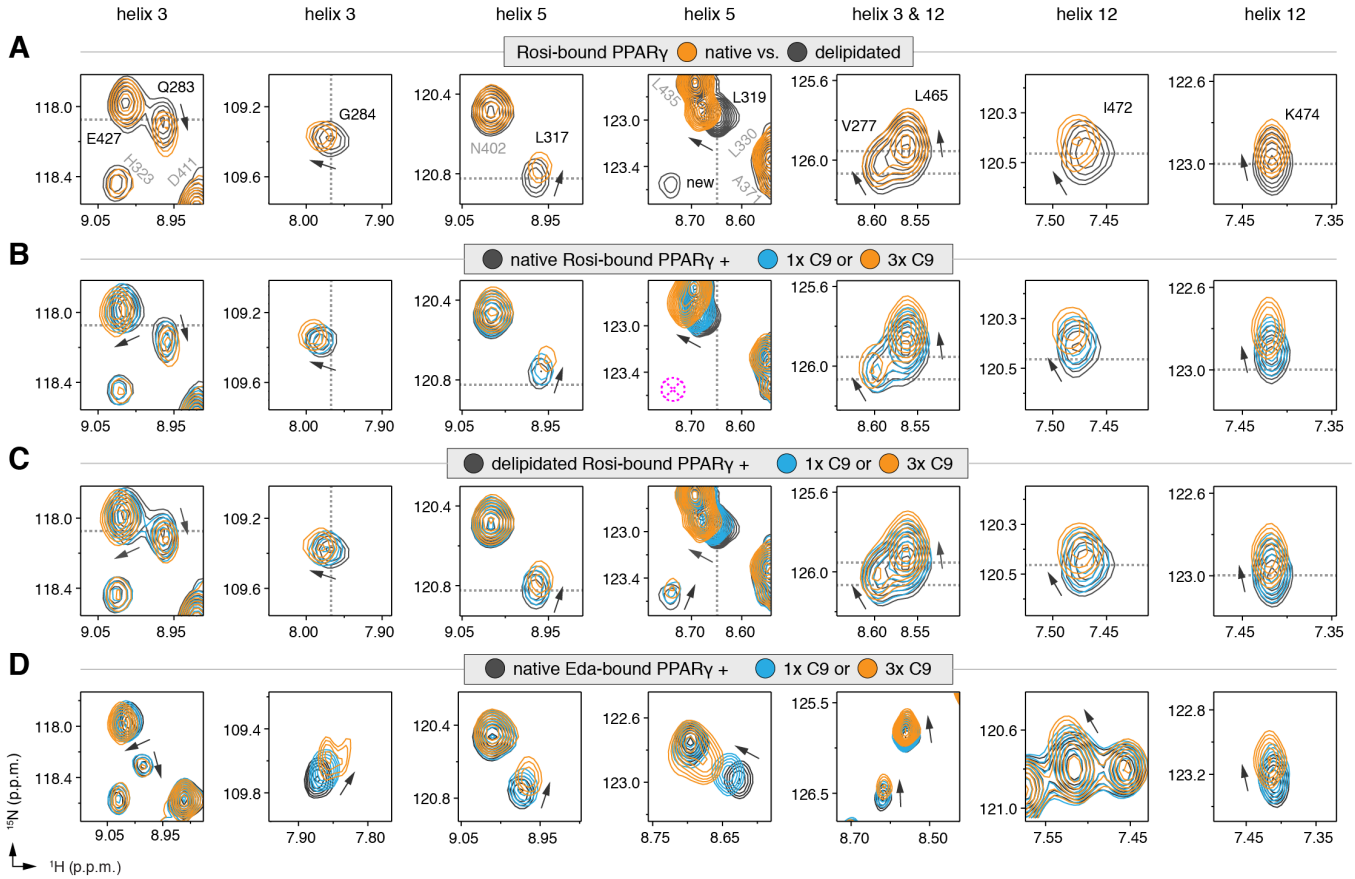

Figure 5. NMR confirms cobinding of exogenously added C9 and synthetic TZDs. Differential 2D [^{1}H,^{15}N]-TROSY-HSQC NMR data comparing (**A**) native vs. delipidated PPARγ LBD bound to rosiglitazone (2 equiv.); (**B**) C9 added into native PPARγ LBD bound to rosiglitazone (2 equiv.); (**C**) C9 added into delipidated PPARγ LBD bound to rosiglitazone (2 equiv.); and (**D**) C9 added into native PPARγ LBD bound to edaglitazone (2 equiv.). The dotted lines in panels A–C represent the vertical (^{1}H chemical shift) or horizontal (^{15}N chemical shift) position of the peaks in the delipidated form to illustrate how the peaks corresponding to the native, nondelipidated form shift "on path" to changes caused by C9 binding. Black arrows denote the chemical shift changes; pink dotted circle/cross denotes a missing peak; and dotted lines denote the delipidated apo-PPARγ peak positions to illustrate the "on path" transitions of native and C9-bound forms.

tense peaks in the delipidated form (**Figure 5A**; "new" label). In our previous NMR analysis of rosiglitazone-bound PPARγ (39), we were unable to assign these peaks due to their weak and/or absent peaks in 3D NMR data, likely due to the substoichiometric cobinding of bacterial MCFAs.

We next performed differential NMR analysis to determine if exogenously added MCFAs, which are dietary components of the mammalian diet, can cobind with synthetic ligands to PPARγ. We titrated C9 into rosiglitazone-bound native PPARγ (**Figure 5B**) and delipidated PPARγ (**Figure 5C**) and again performed differential NMR analysis. The binding affinity of C9 (**Supplementary Figure 6**) is ~50,000-fold weaker than rosiglitazone; thus, to eliminate competition for the orthosteric pocket, we titrated one and three molar equivalents of C9 into PPARγ pretreated with two molar equivalents of rosiglitazone. This analysis again revealed subtle NMR chemical shift perturbations for essentially the same residues that were affected in the differential analysis of rosiglitazone bound to native or delipidated forms without added C9 (**Figure 5A**). Notably, the direction of the chemical shift change that occurs upon titration of C9 to rosiglitazone-bound native (**Figure 5B**) or delipidated (**Figure 5C**) PPARγ is the same direction of the shift that occurs when comparing rosiglitazone-bound native and delipidated PPARγ without added C9 (**Figure 5A**). In fact, the peak position of rosiglitazone-bound native PPARγ shows a "head start" in shifting compared to delipidated PPARγ, which further supports that native rosiglitazone-bound PPARγ is bound to a substoichiometric amount of MCFA. We observed a similar shifting of peaks for edaglitazone-bound PPARγ (**Figure 5D**).

If C9 was competing with rosiglitazone bound to the orthosteric pocket, residues near the TZD head group such as H323, which forms a side chain-mediated hydrogen bond with the aromatic TZD head group, would likely shift significantly. Aromatic ring current effects, which have a significant influence on NMR peak positions, would change in this portion of the orthosteric pocket if C9 displaced rosiglitazone. However, only very minor shifting is observed for the H323 NMR peak as compared to the larger shifting that occurs for residues near the bound C9 in our crystal structure. Furthermore, other NMR peaks affected by C9 binding to PPARγ in the absence of rosiglitazone are not affected in the cobinding experiments with rosiglitazone, nor do they move from the rosiglitazone-bound peak position to the C9-bound peak position (**Supplementary Figure 7**). These observations support the cobinding of C9, not orthosteric competition of C9, under our experimental conditions.

Molecular simulations reveal conformational effects afforded by ligand cobinding

Our NMR results indicate that C9 cobinding to the alternate site when a TZD is bound to the orthosteric pocket can affect the conformation of the AF-2 surface. We performed molecular simulations to determine the potential conformational consequences of the cobinding

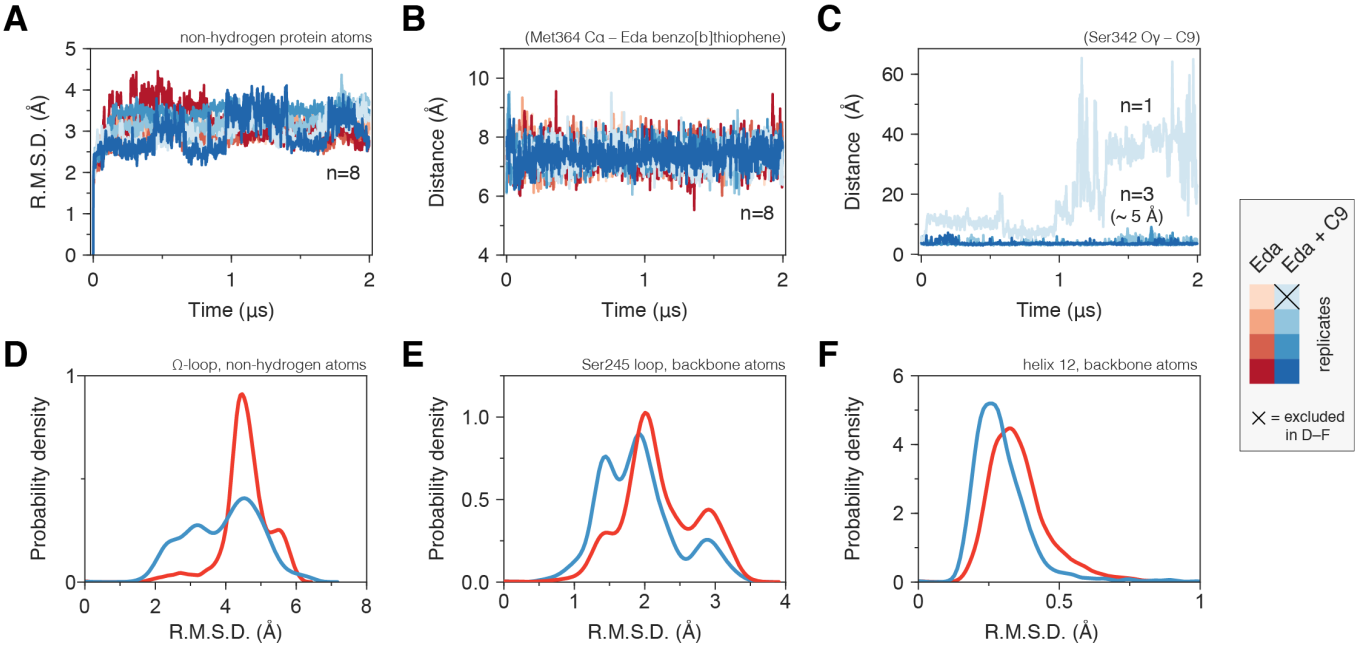

Figure 6. Molecular simulations reveal C9 cobinding stabilizes the PPARγ LBD. (**A**) Heavy atom R.M.S.D. to the starting conformation (crystal structure after minimization and equilibration) reveal that all four simulations bound to edaglitazone only to the orthosteric site (red lines) or cobound to C9 at the alternate site (blue lines) are stable during the simulation period. (**B**) Distance between benzo[b]thiophene group in edaglitazone and the M364 Cα atom shows that edaglitazone remains stably bound to the orthosteric pocket in all eight simulations. (**C**) C9 remains stably bound to the alternate site in three of four cobound simulations. In the legend, × denotes the Eda + C9 (light blue) simulation where C9 unbound during the simulation, which was excluded from the analysis. (**D–F**) Probability density histogram distributions of the R.M.S.D. relative to the starting structure for (**D**) the Ω-loop, (**E**) the loop containing the serine residue phosphorylated by Cdk5, and (**F**) helix 12.

of edaglitazone and C9. Two microsecond simulations were conducted with edaglitazone bound to the orthosteric pocket in the absence or presence of C9 at the alternate site. For each ligand-bound state, two replicate simulations on the chain A and B crystallized conformations were performed resulting in a total of eight stable simulations (**Figure 6A**) allowing averaging of up to four simulations for each state. In all eight simulations, edaglitazone remained stably bound to the orthosteric pocket (**Figure 6B**). C9 remained stably bound to the alternate site in three out of four simulations with edaglitazone cobound to the orthosteric pocket (**Figure 6C**). The simulation where C9 exchanged out of the alternate site was therefore excluded from the analysis.

The conformation of the Ω-loop has been shown to be important in regulating the conformation of helix 12, a critical structural element in the AF-2 surface (13, 14, 40, 41). Conformational fluctuations in the Ω-loop when bound to edaglitazone alone, calculated as the coordinate R.M.S.D. relative to the crystallized conformation after minimization and equilibration, range between 4–6 Å (**Figure 6D**). However, when cobound to C9, Ω-loop conformational fluctuations show a broader range of smaller R.M.S.D. values (2–5 Å) with a notable increase in the 2–4 Å range relative to edaglitazone bound alone. Thus, a conformational stabilizing effect is observed for Ω-loop residues that contact the bound C9. The loop connecting helix 1 and helix 2a, which is proximal to the Ω-loop and contains a residue (S245 in PPARγ1; S273 in PPARγ2) that is phosphorylated by the kinase Cdk5 (26), also shows reduced conformational fluctuation when cobound to C9 relative to edaglitazone bound alone (**Figure 6E**). NMR analysis reveals that C9 cobinding with rosiglitazone or edaglitazone affects the conformation of residues near S245 (**Supplementary Figure 8**). These observations support studies showing that ligand occupancy of the alternate site can affect the conformation of this surface and inhibit Cdk5-mediated phosphorylation of S245 (25). Finally, C9 cobinding to the alternate site stabilizes the conformation of helix 12, which shows decreased R.M.S.D. values relative to edaglitazone bound alone (**Figure 6F**). This is consistent with our NMR data (**Figure 5**) showing that cobinding of C9 with rosiglitazone or edaglitazone affects NMR peaks for residues within the helix 12/AF-2 surface.

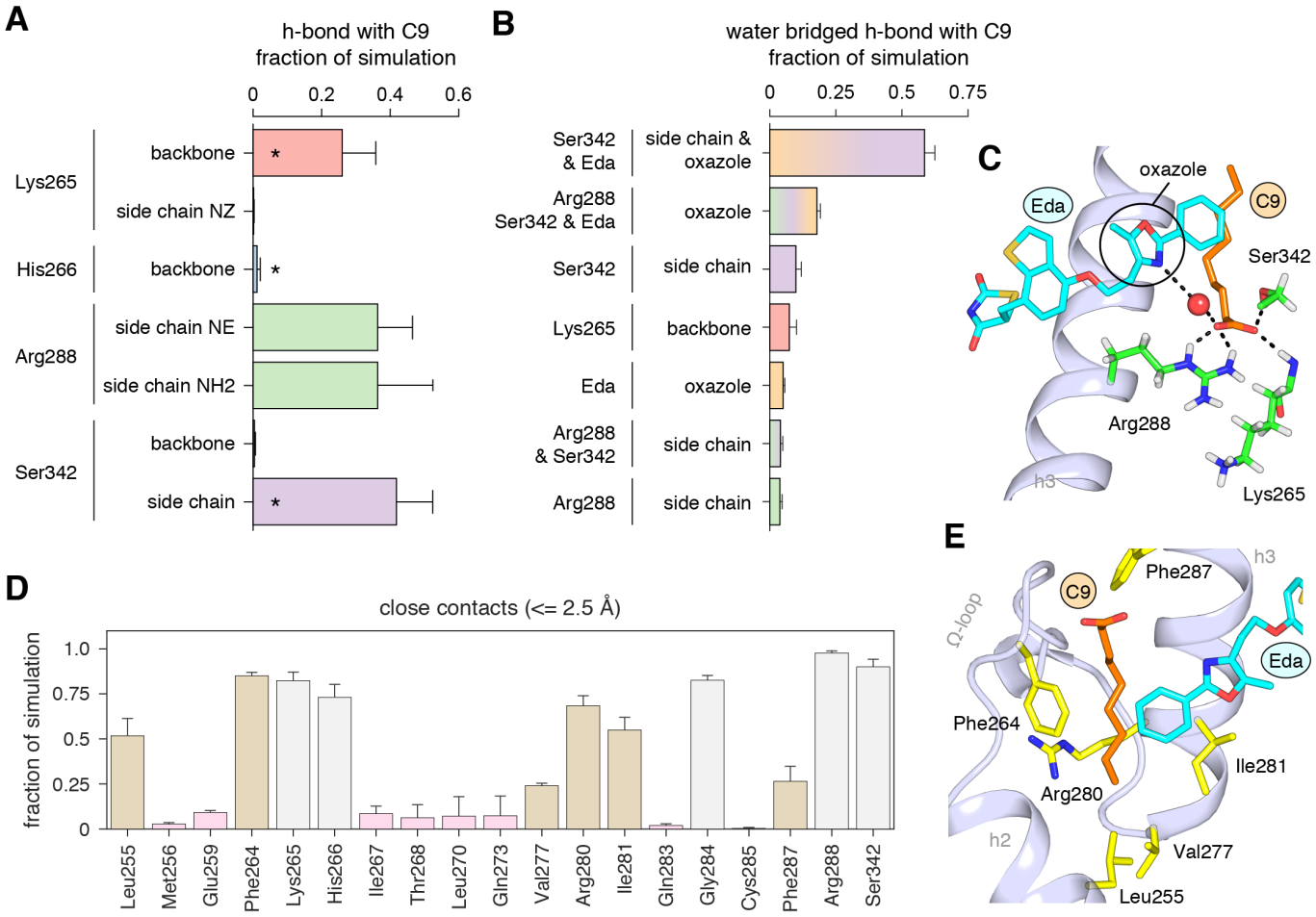

Figure 7. Interactions driving cobinding of C9 to the alternate site. (**A**) Direct and (**B**) water-bridged hydrogen bonds detected in the three 2 μs molecular simulations where C9 remained stably bound; * denotes hydrogen bonds observed in crystal structure. Data plotted as the average and S.D. of three experimental replicates. (**C**) Example of the C9-mediated hydrogen bond network from a snapshot of the simulation trajectory. (**D**) Close atomic contacts populated in the simulation (brown, hydrophobic side chain contacts; grey, other contacts; pink, lower abundance contacts). Data plotted as the average and S.D. of three experimental replicates. (**E**) Structural example of the hydrophobic contacts (brown in **D**).

We analyzed the hydrogen bond network in the molecular simulations to establish the binding determinants of C9 cobinding with edaglitazone. Several hydrogen bonds between the carboxylate head group of C9 and various backbone and side chain groups of PPARγ were observed in all three simulations (**Figure 7A**), and among these the hydrogen bonds to the K265 backbone and S342 side chain were also observed in the crystal structure. The hydrogen bond to the H266 backbone observed in the crystal structure was lowly populated in the simulation, and new hydrogen bonds were detected with the R288 side chain. Notably, a complex network of water-bridged hydrogen bonds was observed (**Figure 7B**), including several different types of water-mediated hydrogen bonds linking the oxazole nitrogen atom in edaglitazone to the carboxylate head group of C9 (**Figure 7C**). In addition to these hydrogen bonds, a network of hydrophobic interactions was observed in all three simulations (**Figure 7D**), including the side chains of L255, F264, V277, R280, I281, F287, and the terminal phenyl group of edaglitazone interacts with the saturated carbon side chain of C9 (**Figure 7E**).

Isolation of MCFA cobinding with covalent orthosteric antagonists

GW9662 (**Supplementary Figure 9**) is an antagonist that covalently binds to C285 located in, and blocks ligand binding to, the orthosteric pocket (42). Structural superposition of an available crystal structure of GW9662-bound PPARγ (PDB: 3B0R) with a crystal structure of PPARγ bound to C9 (32) (PDB: 4EMA) revealed that GW9662 overlaps with two out of the three crystallized C9 binding modes in branches I and III (**Figure 8A**). We solved two new crystal structures of PPARγ bound to GW9662 and SR16832 (23), an analog of GW9662 that we developed with a ligand extension that weakens synthetic ligands binding to the alternate site (23), at 2.29 Å and 2.73 Å, respectively (**Supplementary Table 1**). Similar to our edaglitazone crystal structure, we observed electron density consistent with a bound bacterial MCFA in both structures, which we modeled as C9. In chain A of our GW9662-bound structure, one C9 is present within the branch II region of the orthosteric pocket; in chain B, there are two C9 molecules present, one in branch II and another closer to the cobound position in our edaglitazone structure

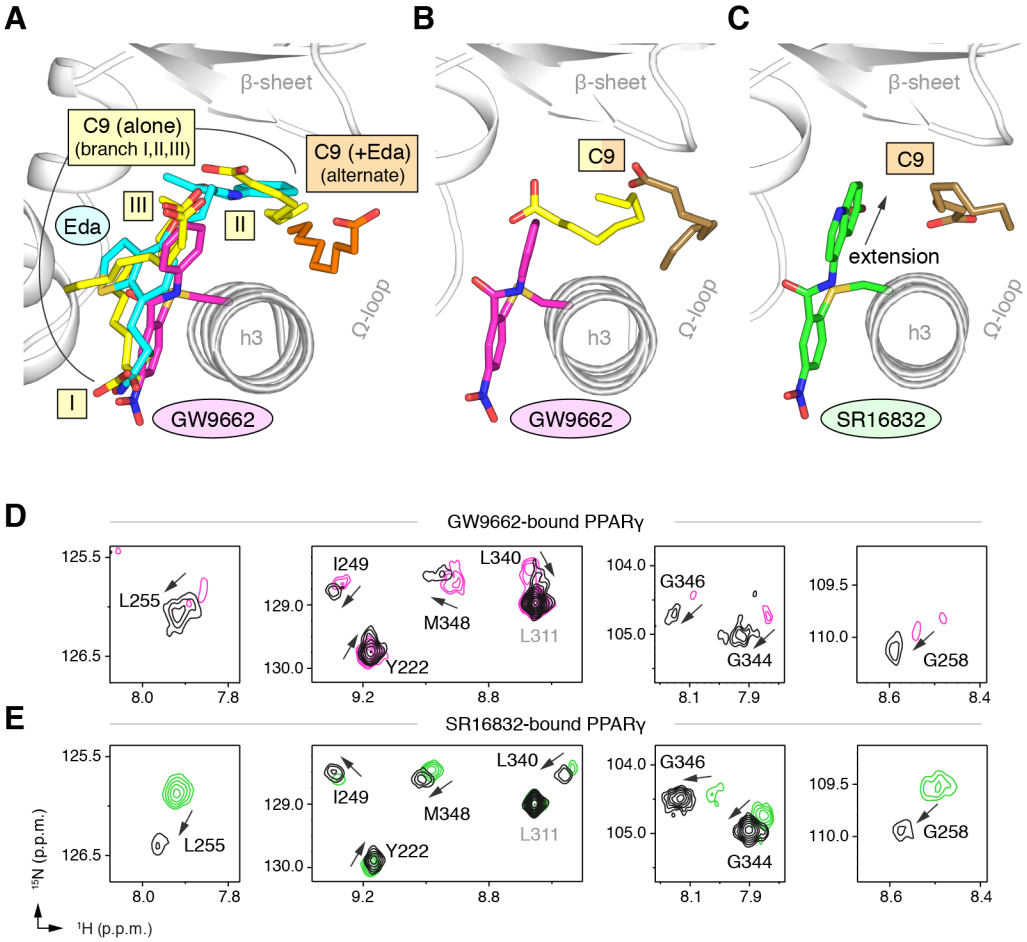

Figure 8. Covalent orthosteric antagonists isolate C9 cobinding. (**A**) The covalent antagonist GW9662 (PDB: 3B0R; magenta) overlaps with the crystallized binding modes of 2 out of 3 C9 molecules bound to the orthosteric pocket (PDB: 4EM9) but not C9 bound to the alternate site. (**B,C**) Crystal structures of PPARγ LBD bound to covalent antagonists (**B**) GW9662 and (**C**) SR16832 cobound to C9. (**D,E**) Differential 2D [^{1}H,^{15}N]-TROSY-HSQC NMR data of PPARγ LBD covalently bound to (**D**) GW9662 (magenta) or (**E**) SR16832 (green) confirms cobinding of C9 (black; 2 equiv.); arrows denote chemical shift changes.

(**Figure 8B; Supplementary Figure 10A**). In the SR16832 structure, C9 is present only in chain A; and the 6-methoxyquinoline group extension in SR16832, relative to GW9662, appears to have blocked the branch II C9 binding mode, pushing the C9 closer to the cobound position in our edaglitazone structure (**Figure 8C; Supplementary Figure 10B**).

We performed differential NMR analysis to confirm the C9 binding regions in the crystal structures of PPARγ bound to GW9662 and SR16832. This analysis was limited relative to the analysis we performed above for rosiglitazone and edaglitazone because about half of the expected NMR peaks are missing due to intermediate exchange on the NMR time scale from significant *μs*–ms time scale dynamics present when bound to covalent antagonists relative to agonists that robustly stabilize the dynamics of PPARγ (20, 22, 23, 39, 43). Despite this limitation, chemical shift perturbations were observed for residues near the crystallized C9 binding modes observed in the GW9662 (**Figure 8D**) and SR16832 (**Figure 8E**) crystal structures, including residues on helix 2b/β-sheet surface such as I249, L255, G258, L340, G344, G346, and M348, confirming the crystallized C9 binding modes.

Cobinding of endogenous UFA and synthetic PPARγ ligands

Our observations described above of fatty acid cobinding were initially made due to the serendipitous retainment of bacterial fatty acids during purification. However, we also showed that addition of exogenous MCFAs, which are mammalian dietary natural ligands, can indeed cobind with synthetic PPARγ ligands. We therefore wondered whether UFAs such as arachidonic acid (AA) and oleic acid (OA), which are endogenous PPARγ ligands (10), could also cobind with synthetic ligands. Although these UFAs have longer carbon chains compared to MCFAs, they can bend and bind in more compact conformations.

To explore this hypothesis, we cocrystallized PPARγ LBD with AA or OA and solved two structures to 2.1 and 1.95 Å, respectively (**Supplementary Table 1**). The structures show two different UFA binding modes in the two chains present in the crystal structure (**Supplementary Figure 11A**): one where the acid group associates near helix 12 with the hydrophobic fatty acid tail projecting to the back portion of the pocket near the β-sheet surface (**Figure 9A,B**); and a second where the acid head group adopts a different conformation flipped away from helix 12 with a similar hydrophobic tail conformation near the β-sheet (**Supplementary Figure 12A,B**). To determine if a synthetic ligand can cobind

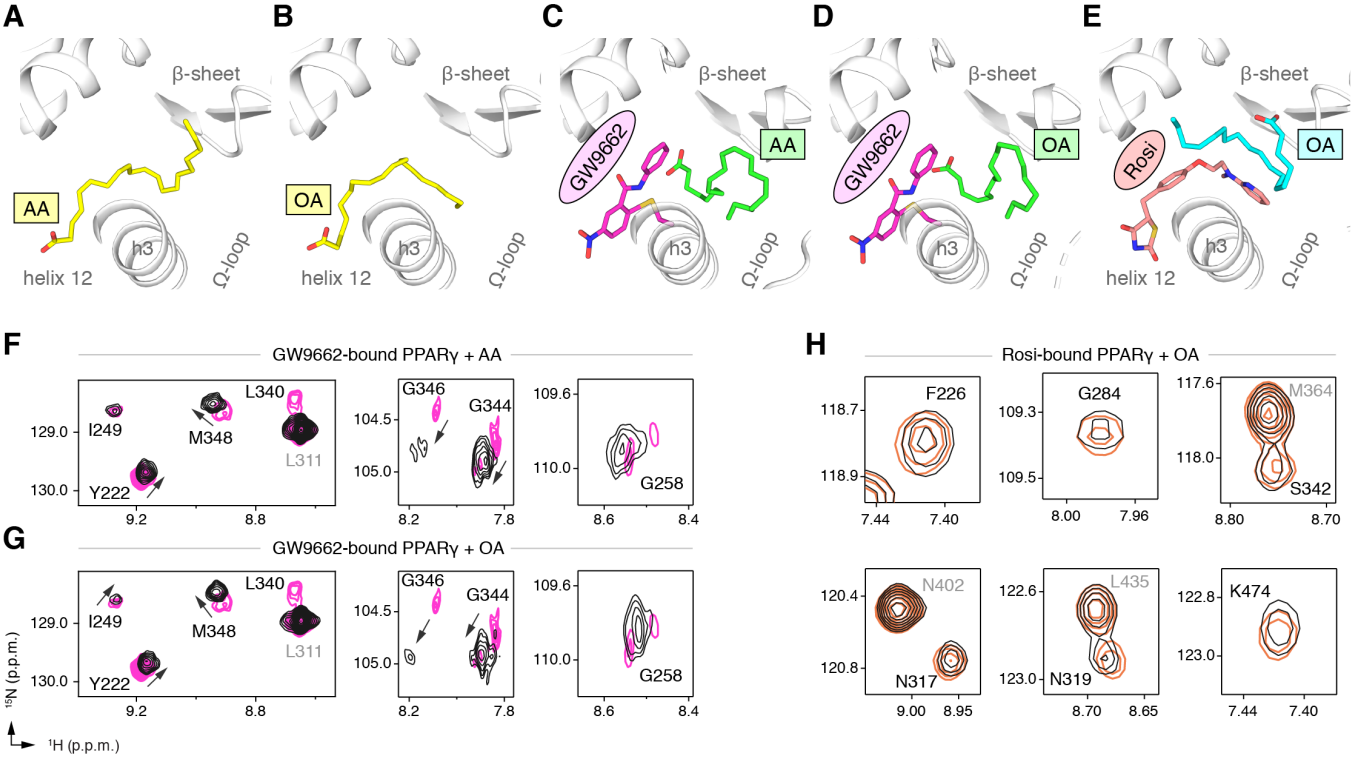

Figure 9. Cobinding of endogenous UFAs and synthetic PPARγ ligands. (**A,B**) UFA ligand binding poses in crystal structures of PPARγ LBD (chain A) bound to (**A**) AA and (**B**) OA. (**C–E**) Ligand binding poses in crystal structures obtained from UFA-bound co-crystals soaked with synthetic ligands, including (**C**) AA-bound PPARγ LBD soaked with GW9662, (**D**) OA-bound PPARγ LBD soaked with GW9662, and (**E**) OA-bound PPARγ LBD soaked with rosiglitazone. (**F,G**) Differential 2D [^{1}H,^{15}N]-TROSY-HSQC NMR data of PPARγ LBD covalently bound to GW9662 (magenta) confirming cobinding with (**F**) AA (black; 1 equiv.). and (**G**) OA (black; 1 equiv.). (**H**) Differential 2D [^{1}H,^{15}N]-TROSY-HSQC NMR data of PPARγ LBD bound to rosiglitazone (pink; 2 equiv.) confirming cobinding with OA (black; 1 equiv.). Black arrows denote the chemical shift changes in the NMR data.

with the bound UFA, we soaked GW9662 or rosiglitazone into preformed UFA-bound crystals and were able to solve three crystal structures to ~2.2 Å (**Supplementary Table 1**), including AA-bound PPARγ with GW9662 (**Figure 9C**), OA-bound PPARγ with GW9662 (**Figure 9D**), and OA-bound PPARγ with rosiglitazone (**Figure 9E**). The structures revealed that the binding of GW9662 or rosiglitazone did not completely displace the bound endogenous UFA (AA or OA). Instead, the binding of the synthetic ligands to UFA-bound PPARγ within the crystals pushed the bound UFA towards the back of the pocket towards the Ω-loop.

We performed differential NMR analysis to confirm the ligand cobinding observed in the crystal structures. When PPARγ is bound to GW9662, addition of AA (**Figure 9F**) or OA (**Figure 9G**) caused selective NMR chemical shift perturbations for a similar set of residues affected in the C9 cobinding NMR experiments. Furthermore, NMR analysis showed that addition of OA to rosiglitazone-bound PPARγ (**Figure 9H**) also caused selective chemical shift perturbations for residues in close proximity to the cobound OA molecule, including F226, G284, and S342; as well as residues within the AF-2 surface on helix 5 (L317 and K319) and helix 12 (K474).

Fatty acid cobinding with synthetic covalent ligands affects coactivator interaction

To determine if cobinding of fatty acid and synthetic ligands can affect PPARγ function, we first performed a TR-FRET biochemical assay that enables measurement of a ligand concentration-dependent change in the binding of a peptide derived from the TRAP220 coactivator protein. In this assay format, we reasoned it would be difficult to differentiate orthosteric competition from cobinding using noncovalent synthetic ligands (i.e., TZDs) when titrating MCFAs and UFAs. We therefore performed experiments using PPARγ LBD without and with preincubation of GW9662 or SR16832, the covalent binding synthetic orthosteric ligands we used to structurally observe fatty acid cobinding in our crystal structures and NMR studies above. To test the functional effect of residues implicated in the C9 cobinding, we generated several mutants. We tested R288A, S342A, and R288A/S342A since these residues directly hydrogen bond via side chain atoms to the cobound C9 ligand in the molecular simulations. Our simulations also revealed a hydrogen bond between C9 and the K265 backbone amide. Because our edaglitazone-bound structure revealed a hydrogen bond between the K265 (Ω-loop) and E291 (helix 3) side chains, which could be

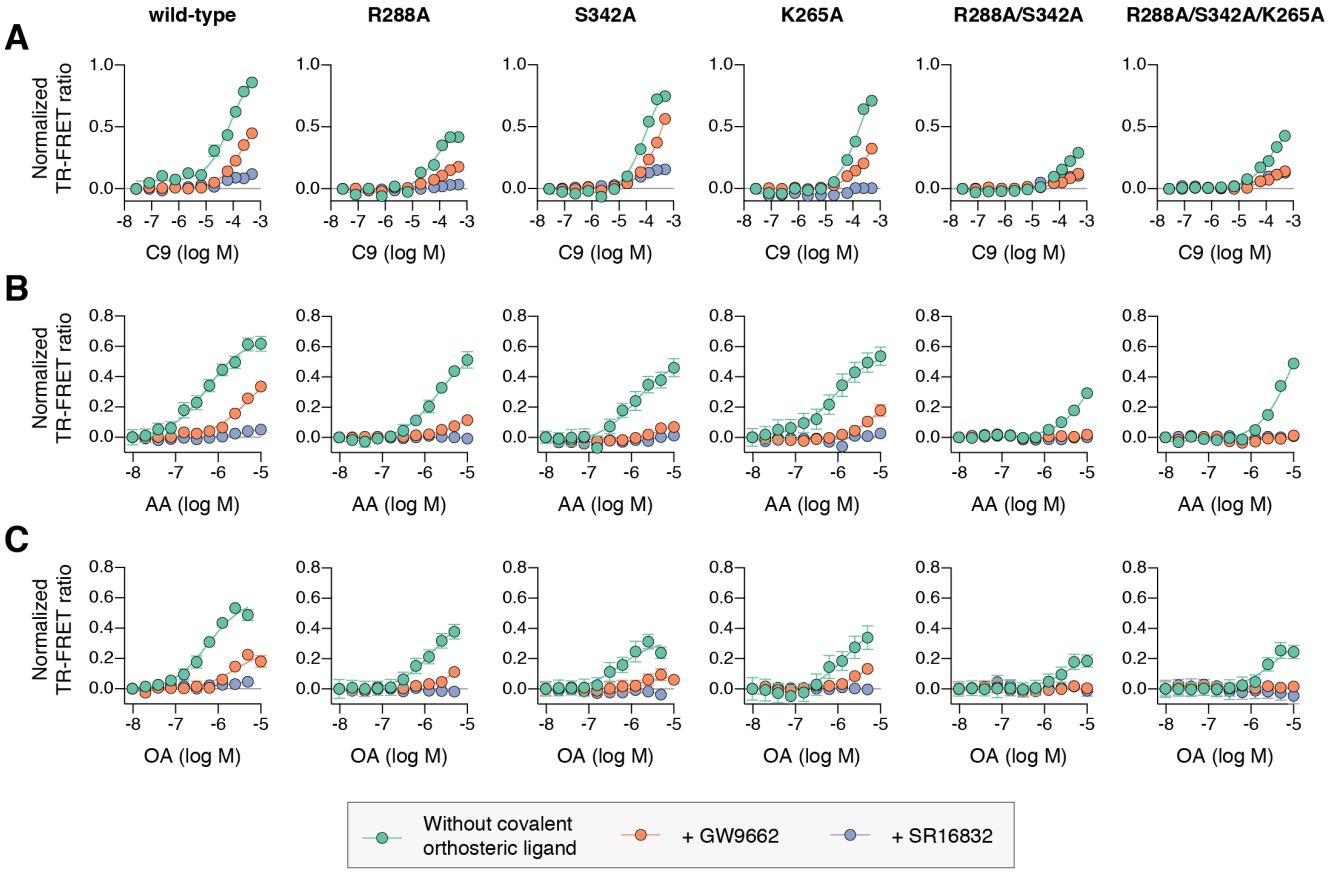

Figure 10. Effect of ligand cobinding of a covalent orthosteric synthetic ligand with MCFA or UFA ligands on PPARγ-coactivator recruitment. TR-FRET biochemical assays showing concentration-dependent changes in the recruitment of a peptide derived from the TRAP220 coactivator for (**A**) C9, (**B**) AA, and (**C**) OA. Experiments were performed in the absence or presence of a covalent orthosteric synthetic ligand; and for wild-type PPARγ LBD or mutant variants; as indicated. Data plotted as the average and S.E.M. of three experimental replicates.

important for stabilizing the Ω-loop, we generated K265A and R288A/S342A/K265A mutants to assess the effect of destabilizing the Ω-loop on C9 binding.

In the TR-FRET assay, the overall window of activity is related to the change in binding affinity of the coactivator peptide; a larger increase in the assay window indicates a larger change in affinity. Because coregulator binding affinity is influenced differently by covalent ligands (23), which causes differences in the basal TR-FRET response (i.e., at low ligand concentrations or DMSO control), we normalized the TR-FRET ratio to easily compare the ligand cobinding and the change in the assay window among the conditions tested.

For wild-type PPARγ, three MCFAs including C9 (**Figure 10A**), decanoic acid (C10; **Supplementary Figure 13A**), and dodecanoic acid (C12; **Supplementary Figure 13B**) and two UFAs AA (**Figure 10B**) and OA (**Figure 10C**) caused a concentration dependent increase in the TRAP220 peptide interaction. When PPARγ was preincubated with GW9662, the fatty acids similarly caused a concentration-dependent increase. However, SR16832 preincubation lowered the assay window of activity to a large degree; smaller MCFAs (C9 and C10) only showed a small increase in TRAP220 peptide interaction, whereas C12 and the endogenous UFAs, AA and OA, did not. This is consistent with our previous report showing that SR16832 more effectively inhibits the UFA docosahexaenoic acid (DHA) from binding to PPARγ compared to GW9662 (23). Furthermore, the trends observed in this TR-FRET ligand-dependent recruitment assay are similar to peptide affinity data we measured using fluorescence polarization (FP) assays (**Supplementary Figure 14**). Taken together, these data show that MCFAs and UFAs binding to PPARγ when orthosteric pocket is blocked by a covalent ligand can influence PPARγ function.

Interestingly, compared to wild-type PPARγ or GW9662-bound PPARγ, we found that C9 binding was more potent for SR16832-bound PPARγ (**Supplementary Figure 15**) despite the bulkier addition in SR16832, relative to GW9662, that points towards and blocks the branch II C9 binding mode (23). Inspection of the SR16832 crystal structure cobound to C9 indicated the increased potency is likely due to hydrogen bonds between the aryl ether/methoxy group of SR16832 with the carboxylate head group and other aliphatic protons in C9 (**Supplementary Figure 16**), the latter of which can form weak hydrogen bonds with methoxy groups (44). In support of this hydrogen bond network, we performed density functional theory (DFT) calculations, which revealed a net attractive interaction between C9 and the SR16832 methoxy group (10.3 kcal/mol) and a repulsive interaction with the phenyl moiety of GW9662 (8.56 kcal/mol).

We next tested C9 and the UFAs with the mutants that we predicted may impact fatty acid cobinding in the TR-FRET assay, including in the presence of the covalent ligands to isolate the impact of the mutants on alternate site binding. For C9, the R288A mutant (**Figure 10A**) decreased the efficacy (i.e., TR-FRET window) more than the other single mutants without affecting potency to a large degree relative to wild-type PPARγ. However, the R288A/S342A double mutant and the R288A/S342A/K265A triple mutant decreased both the potency and efficacy. For AA (**Figure 10B**) and OA (**Figure 10C**), the potency and efficacy was largely affected in the presence of the covalent ligands with the single mutants, and overall most affected for the double and triple mutants. This indicates these residues are important for driving alternate site affinity and/or functional efficacy of cobound UFAs.

UFA cobinding synergizes with synthetic TZD ligands to affect coactivator interaction

We used isothermal titration calorimetry (ITC) analysis to determine if there is a functional effect caused by the ligand cobinding scenarios that we captured in our PPARγ crystal structures bound to the noncovalent synthetic TZD ligands edaglitazone (cobound to C9) and rosiglitazone (cobound to OA); and the apparent C9 density present in a previous rosiglitazone-bound structure (PDB: 1FM9) (35). Importantly, the nature of ITC experiment allows nearly complete control of the experimental setup, in particular the ability to precisely define the components of the assay (e.g., stoichiometry of UFA and TZD ligands in the sample cell). This is not possible in cellular assays, for example, due to the presence of endogenous cellular ligands that cannot be strictly controlled.

In the ITC experiments, we titrated the TRAP220 coactivator peptide into the sample cell containing PPARγ LBD (**Supplementary Figure 17**) to determine how ligand cobinding affected the TRAP220 peptide binding affinity and interaction thermodynamics (**Table 1**). The affinity of the TRAP220 peptide was strengthened in the presence of C9 alone, and more so for OA alone. Inspection of the fitted thermodynamic parameters shows this is driven by a favorable change in entropy (ΔS) in the fatty acid-bound state. In the presence of edaglitazone or rosiglitazone alone, TRAP220 peptide affinity was similarly strengthen driven by a favorable change in entropy with binding affinities similar to OA-bound PPARγ. In the fatty acid cobound scenarios, a synergetic strengthening of TRAP220 peptide affinity was observed, more than in the presence of each ligand individually, which was also driven by a favorable change in entropy. The entropic-driven nature of the cobinding influence on TRAP220 binding is consistent with our NMR and MD data, which indicate that C9 cobinding with an orthosteric TZD stabilizes the conformation of the AF-2 binding surface. These ITC data confirm that ligand cobinding of a noncovalent synthetic ligand with natural or endogenous ligand affects PPARγ function.

Table 1. ITC analysis of TRAP220 peptide titrated into PPARγ LBD.

Ligand	log Ka	Kd (μM)	ΔG (kcal mol^{-1})	ΔH (kcal mol^{-1})	TΔS (kcal mol^{-1})	n (from 2 replicates)
DMSO	4.60 (*4.53, 4.66*)	25.29 (*21.65, 29.77*)	-6.271	-10.53 (*-11.58, -9.70*)	-4.257	0.907, 1.088
C9 (3x)	5.71 (*5.61, 5.82*)	1.94 (*1.53, 2.46*)	-7.793	-10.40 (*-11.10, -9.81*)	-2.612	1.059, 1.087
OA (2x)	5.90 (*5.82, 5.97*)	1.27 (*1.07, 1.51*)	-8.043	-9.24 (*-10.18, -8.31*)	-1.192	1.276, 1.229
Edaglitazone	5.90 (*5.84, 5.96*)	1.26 (*1.10, 1.42*)	-8.051	-10.04 (*-10.24, -9.84*)	-1.992	0.907, 0.863
Rosiglitazone	5.89 (*5.88, 5.94*)	1.28 (*1.13, 1.43*)	-8.042	-8.88 (*-9.04, -8.72*)	-0.838	0.907, 0.909
Edaglitazone + C9	6.20 (*6.10, 6.30*)	0.63 (*0.50, 0.78*)	-8.457	-9.71 (*-9.98, -9.44*)	-1.254	0.840, 0.922
Rosiglitazone + C9	6.24 (*6.16, 6.34*)	0.57 (*0.46, 0.69*)	-8.523	-9.12 (*-9.38, -8.87*)	-0.596	0.939, 0.952
Rosiglitazone + OA	6.16 (*6.02, 6.31*)	0.69 (*0.49, 0.95*)	-8.406	-7.92 (*-8.45, -7.46*)	0.487	1.210, 1.258

Data represent values from an unbiased global fitting of two independent ITC experiments per condition. The 68.3% confidence interval from global fitting listed as italicized values in parentheses when applicable. Stoichiometry (n value) is listed for each independent experiment. Ligands were present at the following molar equivalents: 1 equiv. (edaglitazone and rosiglitazone), 2 equiv. (OA), or 3 equiv. (C9).

Ligand cobinding may synergistically affect cellular PPARγ transcription

Given our data above showing structural and functional synergy in the cobinding of enodgenous UFAs and synthetic TZDs to PPARγ, we sought to determine if cobinding could synergistically affect PPARγ transcription in cells. We approached these studies understanding that ligand conbinding in cells is difficult to robustly prove. It is not possible to quantitatively control many assay parameters in cells, in particular defining which ligands are present (or not), in a manner that can be done in the biochemical assays as well as crystallography and NMR structural experiments that we performed above.

AA and OA, which we used in our structural and biochemical studies above, were among several UFAs identified using a mass spectrometry metabolomics approach as endogenous ligands present in 3T3-L1 preadipocyte cells and mouse brain and adipose tissue that bind to PPARγ (10). Our TR-FRET data confirmed that AA and OA bind to the PPARγ LBD and showed these UFAs cause recruitment of coactivator peptide. However, when we added exogenous AA and OA to cells, no change in PPARγ transcription was observed (**Figure 11A**). These observations together indicate that the exogenously added UFAs are already present within cells, which contributes to the basal PPARγ transcriptional activity in the absence of an exogenous ligand; therefore the exogenously added UFAs cause no further increases in PPARγ transcription. Thus, when we performed cell-based transcriptional assays, we considered the results with the premise that PPARγ will be bound to and activated by endogenous ligands present within the cells.

To determine if endogenous ligands within cells may cobind with TZDs and synergistically affect PPARγ transcription, we compared the transcriptional activities of wild-type PPARγ to single, double, and triple mutant variants that showed reduced UFA-induced coactivator recruitment in the TR-FRET biochemical assay. In cells treated with DMSO control, both mutants showed lower basal transcriptional activity (**Figure 11B**) without affecting PPARγ protein levels in cells (**Supplementary Figure 18**) or coactivator affinity (**Supplementary Figure 19**). When considered with our biochemical studies, this suggests that the mutants may reduce the binding of and activation by endogenous ligands present in cells.

We next determined how the mutants affected the ability of the synthetic TZD ligands to increase PPARγ transcription. Relative to wild-type PPARγ, the mutants showed reduced activity when cells were treated with saturating synthetic TZD concentrations (**Figure 11B**). The reduction in activity caused by the mutants is not due to decreased TZD affinity because concentration-dependent experiments showed that TZD potency was similar for wild-type PPARγ and the mutants (**Figure 11C**). Furthermore, whereas the overall activation at saturating TZDs levels is lower for the mutants, concentration-dependent relative window of TZD efficacy is similar for wild-type PPARγ and the mutants. When considered with all of the above studies, these data indicate that cobinding of endogenous ligands and synthetic TZDs may synergistically activate PPARγ transcription over the activity of a single ligand alone.

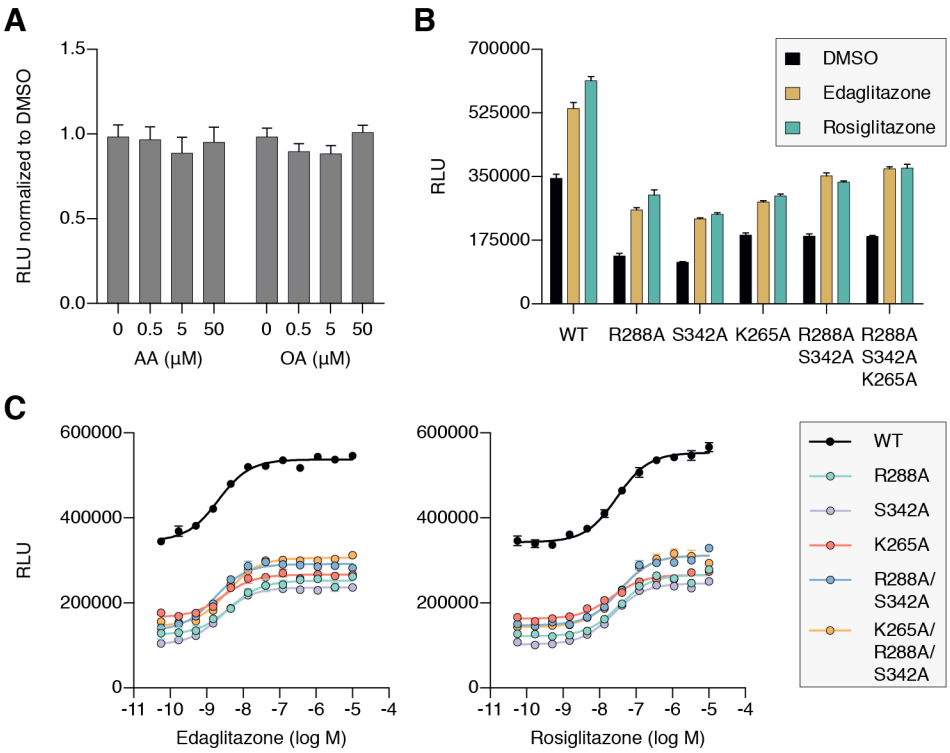

Figure 11. Cellular activation of PPARγ by TZDs may be influenced by cobinding of endogenous ligands. (**A**) Luciferase reporter assay measuring full-length wild-type PPARγ transcription in HEK293T cells treated with exogenously added UFAs, which are endogenous ligands present in cells. (**B,C**) Luciferase reporter assay measuring full-length wild-type and mutant PPARγ transcription in HEK293T cells treated with ligand in (**B**) single-point (10 μM) and (**C**) dose-response format. Data plotted as the average and s.e.m. of four experimental replicates; dose response data were fit to a sigmoidal dose response equation. Fitted EC_{50} values are similar for wild-type and the mutant variants for edaglitazone (2–4 nM) and rosiglitazone (22–36 nM).

DISCUSSION

Synthetic ligands and FDA-approved anti-diabetic drugs that target the nuclear receptor PPARγ are thought to compete with and completely displace (i.e., cause unbinding of) natural/endogenous ligands upon binding to an orthosteric pocket to regulate PPARγ activity. This competitive or "one-for-one" orthosteric ligand exchange model was developed from crystal structures of PPARγ bound to individual ligands, whereby structural overlay of these structures showed that the ligands have overlapping orthosteric binding modes. Our findings here indicate that this classical nuclear receptor ligand exchange model may be more complex than currently appreciated. To our knowledge, this is the first mechanistic description showing that the binding of a synthetic nuclear receptor ligand binding can push aside and cobind with a pre-bound endogenous ligand. This mechanism is particularly evident in our crystallography studies whereby co-crystals of UFA-bound PPARγ, where the UFA crystallized in the orthosteric pocket, was pushed to an alternate site when the crystals were soaked with synthetic ligand. This ligand cobinding mechanism bridges or extends the reach of synthetic ligand within the orthosteric pocket with residues near and within the flexible Ω-loop region that is important in regulating PPARγ structure and function (13, 14, 24, 25, 40, 41), which is supported by our coregulator interaction assays and particularly our ITC studies that show cobinding of an endogenous UFA and synthetic TZD ligand synergistically improves coactivator affinity compared to each ligand alone. This highlights an important but perhaps underappreciated concept of considering cobinding of natural ligands with designed synthetic ligands in drug discovery efforts.

A growing number of studies have revealed other complex PPARγ ligand binding scenarios. Serotonin and fatty acid metabolites were shown to synergistically bind to different arms of the orthosteric pocket (41). MCFAs and long-chain oxidized fatty acids were also shown bind in up to three equivalents of the same ligand bound to different arms of the orthosteric pocket (11, 32). We have shown that some synthetic ligands optimized to bind to the orthosteric pocket with high affinity can also bind a second equivalent to the alternate site at lower affinity (20-22); or one equivalent to the alternate site with an orthosteric antagonist or an oxidized lipid covalently bound to the orthosteric pocket (22). Similar to our synthetic ligand alternate binding observations, a crystal structure of PPARγ that showed that a plant-based natural product (luteolin) can bind to the alternate site cobound with a bacterial saturated 14-carbon fatty acid (myristic acid) that copurified during protein expression (40). Molecular simulations showed that luteolin bound to the alternate site stabilizes the Ω-loop, and the cobinding is mediated in part through a water bridged hydrogen bond, similar to our cobinding

molecular simulations with edaglitazone bound to the orthosteric pocket and C9 bound to the alternate site. In studies of other nuclear receptors, RORγ was shown to cobind a synthetic ligand and its natural ligand cholesterol, both to the orthosteric pocket (45); while another focused on PXR revealed orthosteric cobinding of a pharmaceutical oestrogen and an organochlorine pesticide (46).

Our observations here, while related to the above studies showing different multiple ligand-bound scenarios, are different. Through a series of crystal structures we mechanistically show that a synthetic PPARγ ligand, including one used as FDA-approved drug in the treatment of type 2 diabetes, pushes a bound endogenous UFA to an alternate site upon binding rather than displacing it. This likely occurs because the synthetic ligand displays higher affinity than the UFA for the orthosteric pocket, but the UFA also has moderate or reasonable affinity, rather than weak or no affinity, for other portions of the pocket (i.e., the alternate site). The cobound fatty acid in the alternate site, which is located near the β-strand surface and Ω-loop region, is structurally close to two other important surfaces. In a crystal structure of the intact PPARγ/RXRα heterodimer bound to DNA (47), there is a long-range interaction between this region in PPARγ and the RXRα DNA-binding domain (DBD). It is possible that ligand cobinding could allosterically affect or synergize with this long-range interaction. Furthermore, the alternate site where the cobound fatty acid is bound is structurally close to a surface containing S245 (S273 in PPARγ isoform 1), which is phosphorylated by the kinase Cdk5 (26). The antidiabetic efficacy of PPARγ-binding ligands is linked to inhibiting this phosphorylation event (26, 27), and occupancy of the alternate site can specifically inhibit this phosphorylation event (25). It is possible that a cobound endogenous ligand at the alternate site may contribute to the antidiabetic efficacy of a synthetic ligand bound to the orthosteric pocket. However, it is difficult to study possible cellular functional effects of synthetic and endogenous ligand cobinding because it is not possible to control the presence of endogenous ligands as one can with synthetic ligands. Our findings may inspire others to develop new techniques or tools determine how to robustly assess the cellular impact of synthetic and endogenous ligand cobinding.

The ligand cobinding mechanism we discovered here for PPARγ may be broadly applicable to other nuclear receptors and other ligand-binding proteins. For example, many nuclear receptors, including ones not normally thought to be fatty acid responsive, have been shown to interact with and/or be functionally modulated by fatty acids. This list not only includes other PPARs, namely PPARα (48-51) and PPARδ (18, 48, 52), but also receptors for retinoids including RXRα (53-56) and RAR (57); steroid hormone receptors including LXRα (58-61), FXR (62), AR (63), TR (64, 65), ER (66, 67), PR (68), and GR (68, 69) including a second non-hormone site in GR (70); as well as orphan receptors including HNF4α (71, 72), Nurr1 (73, 74), Nur77 (75), and TR4 (76). It is possible that synthetic ligands targeting these nuclear receptors also cobind with fatty acids, or even other types of endogenous ligands, with synergistic affects, positive or negative, on receptor function. In fact, fatty acids are considered to the ancestral nuclear receptor ligands (77) and also interact with and regulate the function of a variety of other protein targets including kinases (78-80), GPCRs (81, 82), and ion channels (83, 84) which are targets (or putative targets) of synthetic ligands and clinically used drugs. More broadly, fatty acids and lipids are just one type of endogenous metabolite present in cells and it is estimated that most proteins likely bind endogenous metabolites (85-90). Thus, the concept of synthetic ligand/drug cobinding with endogenous metabolites to targets may be more likely than not.

ACKNOWLEDGEMENTS

This work was supported in part by National Institutes of Health (NIH) grants R01DK101871 (DJK), R00DK103116 (TH), and F32DK108442 (RB); American Heart Association (AHA) fellowship award 16-POST27780018 (RB); National Science Foundation (NSF) funding to the Summer Undergraduate Research Fellows (SURF) program at The Scripps Research Institute [Grant 1659594]; and the Academic Year Research Internship for Undergraduates (AYRIU) program at The Scripps Research Institute.

AUTHOR CONTRIBUTIONS

J.S. and D.J.K. conceived and designed the research. J.S. expressed and purified protein; solved the crystal structures; performed and analyzed NMR and biochemical assays; and analyzed previously solved ligand-bound crystal structures. R.B. and S.A.M. performed cell-based assays. J.B. performed site-directed mutagenesis and expressed/purified protein. P.M.-T. performed biochemical assays. T.S.H. built and performed minimization/equilibration of molecular simulation input files; and provided advice on simulations runs and analyses. M.T. and Q.G. performed density functional theory calculations. D.J.K. performed molecular simulations, analyzed data, supervised the research, and wrote the manuscript with help from J.S. and input from all authors.

COMPETING FINANCIAL INTERESTS

The authors declare no competing financial interests.

METHODS

Materials and reagents

Rosiglitazone, edaglitazone, and GW9662 ligands were obtained from commercial sources (Cayman and

Tocris Bioscience). SR16832 was synthesized in-house as previously described (23). Peptides of LXXLL-containing motifs from TRAP220 (residues 638–656; NTKNHPMLMNLLKDNPAQD) and NCoR (2256–2278; DPASNLGLEDIIRKALMGSFDDK) containing a N-terminal FITC label with a six-carbon linker (Ahx) and an amidated C-terminus for stability were synthesized by LifeTein.

Protein purification

Human PPARγ LBD (residues 203–477, isoform 1 numbering; or residues 231–505, isoform 2 numbering) was expressed in *E. coli* BL21(DE3) cells using autoinduction ZY media or M9 minimal media supplemented with NMR isotopes as a Tobacco Etch Virus (TEV)-cleavable N-terminal hexahistidine(6xHis)-tagged fusion protein using a pET46 Ek/LIC vector (Novagen) and purified using nickel affinity chromatography and size exclusion chromatography. The purified proteins were concentrated to 10 mg/mL in a buffer consisting of 20 mM potassium phosphate (pH 7.4), 50 mM potassium chloride, 5 mM tris(2-carboxyethyl)phosphine (TCEP), and 0.5 mM ethylenediaminetetraacetic acid (EDTA). Purified protein was verified by SDS-PAGE as >95% pure. For studies using a covalent orthosteric antagonist, PPARγ LBD protein was incubated with at least a ~1.05x excess of GW9662 or SR16832 at 4 °C for 24 h to ensure covalent modification to residue C285, then buffer exchanged the sample to remove excess covalent antagonist and DMSO. Complete attachment of the covalent antagonist occurs within 30–60 minutes, as detected using ESI-MS with a LTQ XL linear Ion trap mass spectrometer (Thermo Scientific). For studies using delipidated protein, two protocols were used (LIPIDEX and refolding) that gave similar results. For LIPDEX delipidation, protein was incubated with LIPIDEX-1000 (Perkin Elmer) at 37 °C for 1h and buffer exchanged into the aforementioned phosphate buffer. For delipidation by refolding, protein was first subjected to a chloroform/methanol lipid extraction (91) and the denatured protein was refolded using a fast dilution/dialysis procedure followed by size exclusion chromatography (92). NMR spectra of delipidated protein obtained from both procedures were essentially identical.

TR-FRET ligand displacement and coregulator interaction assays

The time-resolved fluorescence resonance energy transfer (TR-FRET) assays were performed in black low-volume 384-well plates (Greiner). For the ligand displacement assay, each well contained 1 nM delipidated 6xHis-PPARγ LBD protein, 1 nM LanthaScreen Elite Tb-anti-HIS Antibody (Thermo Fisher Scientific), and 5 nM Fluormone Pan-PPAR Green (Invitrogen) in TR-FRET buffer containing 20 mM potassium phosphate (pH 8), 50 mM potassium chloride, 5 mM TCEP, and 0.005% Tween-20 in the absence or presence of ligand in triplicate at a concentration equal to the highest protein concentration to ensure complete formation of ligand-bound protein. For the TR-FRET coregulator assay, each well contained 4 nM 6xHis-PPARγ LBD protein (with or without covalent modification by a covalent antagonist), 1 nM LanthaScreen Elite Tb-anti-HIS Antibody (Thermo Fisher Scientific), and 400 nM FITC-labeled TRAP220 or NCoR peptide described above in TR-FRET buffer. Ligand stocks were prepared via serial dilution in DMSO, added to wells in triplicate, and plates were incubated at 25 °C for 1 h and read using BioTek Synergy Neo multimode plate reader. The Tb donor was excited at 340 nm; its fluorescence emission was monitored at 495 nm, and the acceptor FITC emission was measured at 520 nm; and the TR-FRET ratio was calculated as the signal at 520 nm divided by the signal at 495 nm. Data were plotted using GraphPad Prism as TR-FRET ratio vs. ligand concentration; TR-FRET coregulator data were fit to sigmoidal dose response curve equation, and ligand displacement data were fit to the one site – Fit K_i binding equation to obtain K_i values using the known binding affinity of Fluormone Pan-PPAR Green (2.8 nM; Invitrogen PV4894 product insert).

Fluorescence polarization coregulator interaction assays

Wild-type or mutant 6xHis-PPARγ LBD in assay buffer (20 mM potassium phosphate (pH 8), 50 mM potassium chloride, 5 mM TCEP, 0.5 mM EDTA, and 0.01% Tween-20) was diluted by serial dilution and plated with 200 nM FITC-labeled TRAP220 or NCoR peptides described above in black 384-well plates (Greiner). The plate was incubated at 4 °C for 1 hr, and fluorescence polarization was measured on a BioTek Synergy Neo multimode plate reader at 485 nm emission and 528 nm excitation wavelengths. Data were plotted using GraphPad Prism as fluorescence polarization signal in millipolarization units vs. protein concentration and fit to a one site total binding equation.

Luciferase reporter assays and western analysis of protein levels

For the luciferase reporter assay, HEK293T cells (ATCC; cat# CRL-3216) were cultured in DMEM media (Gibco) supplemented with 10% fetal bovine serum (FBS) and 50 units mL^{-1} of penicillin, streptomycin, and glutamine and grown to 90% confluency in a T-75 flask before seeding 4 million cells per well in 10 cm dishes. Seeded cells were transfected with 4.5 µg of pCMV6-XL4 plasmid containing full-length human PPARγ2 and 4.5 µg of 3X-multimerized PPAR response element (PPRE)-luciferase reporter plasmid with 27 µL of X-treme Gene 9 transfection reagent (Roche) in Opti-MEM reduced serum media (Gibco). Following 18 hr incubation at 37 °C in a 5% CO_2 incubator, transfected cells were plated in white 384-well plates (Perkin Elmer) at a density of 10,000 cells per well (20 µL volume). After plating, cells were incubated 4 hr before treatment in quadruplicate with 20 µL of either vehicle control (2% DMSO in DMEM media) or 1:3 serial dilution of ligand

(edaglitazone or rosiglitazone) from 2 pM– 630 nM; DMSO concentration was constant at 2% in all wells. Following a second 18 hr incubation, treated cells were developed with 20 µL Britelite Plus (Perkin Elmer), and luminescence was measured using a BioTek Synergy Neo multimode plate reader. Data were plotted in GraphPad Prism as luminescence vs. ligand concentration and fit to a sigmoidal dose response curve.

For the western analysis, HEK293T cells (ATCC; cat# CRL-3216) were transfected described above except in 6-well plates (Corning) with 250,000 cells and 1 µg of pCMV6-XL4 plasmid containing wild-type or mutant full-length human PPARγ2 with 3 µL of X-treme Gene 9 and incubated for 48 hr. Transfected cells were then lysed in TNT buffer (150 mM NaCl, 0.1 M Tris, 1% Triton-X 100, pH 7.5) and incubated for 1 hr at 4 ˚C. Protein concentration was determined by BCA assay (ThermoFisher). Protein (20 µg) was loaded onto 4-15% gradient gels (Bio-Rad) and wet transferred onto PVDF. The membrane was blocked for 1 hr at room temperature with 5% milk in PBS. All antibodies were diluted in 1% milk in PBS. After blocking, the membrane was incubated overnight at 4 ˚C with 1:1000 dilution of rabbit anti-PPARγ (Cell Signaling Technology, #2435). The following day, the blot was washed with PBST and treated with 1:3000 dilution of anti-rabbit IgG-HRP (Cell Signaling Technology, #7074) for 45 min at room temperature, then washed with PBST and developed with ECL (ThermoFisher). The membrane was stripped, blocked, and re-probed with 1:1000 mouse anti-actin (EMD/MilliporeSigma, MAB1501) overnight at 4 ˚C. The following day the blot was washed with PBST and treated with 1:10,000 dilution of anti-mouse IgG-HRP (Sigma Aldrich, #A9917) for 45 min at room temperature, then washed with PBST and developed with ECL (Thermo Fisher).

Crystallization, structure determination, and structural analyses

PPARγ LBD protein was purified as described above. For edaglitazone, arachidonic acid, oleic acid and GW9662-PPARγ LBD complexes, protein was incubated at a 1:3 protein/ligand molar ratio in PBS overnight, concentrated to 10 mg/mL, and buffer exchanged. Crystals were obtained after 3–5 days at 22 °C by sitting-drop vapor diffusion against 50 µL of well solution using 96-well format crystallization plates. The crystallization drops contained 1 µL of protein/ligand sample mixed with 1 µL of reservoir solution containing 0.1 M Tris-HCl (pH 7.6) and 0.8 M sodium citrate. Crystals for the GW9662/AA, GW9662/OA, rosiglitazone/OA PPARγ LBD complexes were obtained by soaking GW9662 or rosiglitazone (1mM in reservoir solution containing 5% DMSO) into preformed AA or OA bound PPARγ LBD crystals. Crystals for the SR16832-PPARγ LBD complex were obtained via “dry” co-crystallization method (52) after ~14 days using a reservoir solution containing 0.1 M MOPS (pH 7.6) and 0.8 M sodium citrate. All crystals were flash-frozen in liquid nitrogen before data collection. Data collection for the edaglitazone-bound structure was carried out at LS-CAT Beamline 21-ID-D at the Advanced Photon Source at Argonne National Laboratory; the GW9662-bound structures at Beamline 5.0.2 at Berkeley Center for Structural Biology; and the arachidonic acid, oleic acid and SR16832-bound structures using our home source MicroMax007 HF x-ray generator equipped with the mar345 detector. Data were processed, integrated, and scaled with the programs Mosflm (93) and Scala in CCP4 (94). The structure was solved by molecular replacement using the program Phaser (95) that is implemented in the Phenix package (96) using a previously published PPARγ LBD structure (PDB: 1PRG) (9) as the search model. The structure was refined using Phenix with several cycles of interactive model rebuilding in Coot (97). Figures were prepared using PyMOL (Schrödinger), and the orthosteric pocket and alternate site volumes shown in Figure 1 were calculated using HOLLOW (98).

C9 fitting into published ligand-bound PPARγ crystal structures

We analyzed several high-resolution crystal structures, including structures where based on sequence information it was possible that Ω-loop density was present, to determine if density consistent with a medium chain fatty acid could be present. Our analysis included PDB codes 1fm6, 1fm9, 1k74, 1zgy, 2hfp, 2prg, 2q5s, 2q61, 2q6s, 2q6r, 2zk1, 2zk2, 2zk3, 2zk4, 2zk5, 2zk6, 2zvt, 3adw, 3b0q, 3dzu, 3dzy, 3e00, 3qt0, 3r8i, 3t03, 4ema, 4fgy, 4xld, 5two. In some cases it was assumed that the potential fatty acid electron density may have been fitted by water molecules in the previous structure determinations near the site where we observed a MCFA in our edaglitazone-bound structure. In other cases, we analyzed the electron density present in mtz files downloaded from the PDBe (e.g., http://www.ebi.ac.uk/pdbe/coordinates/files/xxxx_map.mtz; where xxxx is the PDB code in lower case letters) for unmodeled density. After removal of all water molecules from the PDB structure file, a ligand search followed by interactive real space refinement was performed using the crystallography atomic modeling program Coot (97); this structure was subjected to refinement with rebuilt water molecules using Phenix (96). Of the structures analyzed, C9 was successfully fitted into the electron density of PPARγ LBD bound to the TZD ligands rosiglitazone (PDB: 1FM6) and MCC-555 (PDB: 3B0Q), as well as the non-TZD ligands SR145 (PDB: 2Q61) and GQ-16 (PDB: 3T03).

NMR spectroscopy

Two-dimensional (2D) [^{1}H,^{15}N]-transverse relaxation optimized spectroscopy (TROSY)-heteronuclear single quantum correlation (HSQC) data were collected at 298K using a Bruker 700 Mhz NMR instrument equipped with a QCI cryoprobe. Samples contained approximately 200 µM protein in a NMR buffer contain-

ing 50 mM potassium phosphate (pH 7.4), 20 mM potassium chloride, 1 mM TCEP, and 10% D_2O. Data were processed and analyzed using Topspin 3.0 (Bruker) and NMRViewJ (OneMoon Scientific, Inc.) (99). NMR analysis was performed using previously described rosiglitazone-bound NMR chemical shift assignments (BMRB entry 17975) (39); for the analysis of PPARγ bound to edaglitazone and/or C9, the analysis was limited to well resolved peaks for residues with chemical shift values similar to PPARγ bound to rosiglitazone via the minimum chemical shift procedure (100).

Molecular dynamics simulations

Edaglitazone was modeled with the NH in the thiazolidinedione group (pKa ~6.4 (101)) as deprotonated, thus with a total charge of -1 at physiologic pH. C9 (pKa of the carboxyl group is ~5) was modeled as deprotonated and having an overall -1 charge. Appropriate protons were added to edaglitazone and C9 structures extracted from the crystal structure using Chimera (102) and submitted to REDD server (103). The resulting mol2 files were used in tleap (AMBER version 16) along with the crystal structure bound to edaglitazone and C9 (PDB: 5UGM). Missing amino acids were added via Modeller (104) within Chimera, including an N-terminal glycine that was added in order to match the NMR construct (vestige of tag cleavage). The structures (without ligand) were run through the H++ server (105) to calculate probable protonation states of titratable protons based on structure. Ligands were then added to the H++ PDB file via overlay of the crystal structure in Chimera. Pdb4amber was used to generate a PDB file with amber names and antechamber was used to give gaff2 names to the ligand mol2 files. Parmchk2 was used to generate force modification files for the ligands with gaff2 parameters. Sodium ions were used to neutralize the ligand-protein complex, and KCl was added to 50 mM (to match the NMR experimental conditions) using TIP3P specific parameters (106). The system was solvated with TIP3P (107) water in a truncated octahedron box at least 10 Angstroms from any protein or ligand atom. FF14SB (108) was used for protein parameters. This build was then minimized and equilibrated in 9 steps with restraints on heavy atoms decreasing with each step with the last minimization and equilibration steps without restraints. Production runs were then carried out with hydrogen mass repartitioned (109) parameter files to enable 4 fs time steps. Constant pressure replicate production runs were carried out with independent randomized starting velocities. Pressure was controlled with a Monte Carlo barostat and a pressure relaxation time (taup) of 2ps. Temperature was kept constant at 310 K with Langevin dynamics utilizing a collision frequency (gamma_ln) of 3 ps^{-1}. The particle mesh ewald method was used to calculate non-bonded atom interactions with a cutoff (cut) of 8.0 Å. SHAKE (110) was used to allow longer time steps in addition to hydrogen mass repartitioning. Analysis of trajectories was performed using cpptraj (111) and pytraj. Hydrogen bond analysis was performed using dist = 3.5 Å and angle = 100° (112).

Density functional theory calculations

All calculations were performed at B3LYP/6-311 + G (113, 114) level using Gaussian 98 package. In order to reduce the calculation time/computational cost, we used a simplified model by only considering the C9-interacting parts of GW9662 (phenyl group), SR16832 (6-methoxyquinoline group) in the calculations. Geometry optimizations were performed for GW9662, SR16832, C9, GW9662+C9, and SR16832+C9 using the structural conformations present in the crystal structures.

Isothermal Titration Calorimetry

ITC experiments were carried out on a MicroCal iTC200 calorimeter (GE/MicroCal, Northampton, MA) using the iTC200 software (v 1.24.2) for instrument control and data acquisition. PPARγ LBD was present in the sample cell that also contained either 1.5% DMSO (control) or ligand with the weaker binding natural ligand (C9) or endogenous ligand (OA) added in 2 or 3 molar equiv., respectively, relative to the high affinity synthetic ligands (edaglitazone or rosiglitazone) for the following conditions — C9 (3 molar equiv.), OA (2 molar equiv.), rosiglitazone (1 molar equiv.), edaglitazone (1 molar equiv.) — that were diluted to 60 µM in reaction buffer consisting of 20 mM KPO4 (pH 7.4), 50 mM KCl, 5 mM TCEP, 0.5mM EDTA, and 0.5%DMSO. TRAP220 peptide powder was dissolved in the same buffer at 600 µM. The reaction cell contained 60 µM protein-ligand complex (200 µl) was titrated with 0.4 µL pre-injection followed by nineteen 2 µL injections of 600 µM TRAP220. Mixing was carried out at 25 °C with reference power and rotational stirring set at 5 µcal/s and 1200 rpm, respectively. Data were processed in NITPIC (115) to determine binding stoichiometry and further analyzed by unbiased global fitting of two replicate runs per ligand-bound condition in SEDPHAT (116, 117), followed by export to GUSSI for publication-quality figure preparation (118). The SEDPHAT fitting model used was A + B to AB heteroassociation and the fit parameters were enthalpy (ΔH) and affinity (K_d).

REFERENCES

1. Soccio RE, Chen ER, Lazar MA. Thiazolidinediones and the promise of insulin sensitization in type 2 diabetes. Cell Metab. 2014;20(4):573-91.

2. Fujita T, Sugiyama Y, Taketomi S, Sohda T, Kawamatsu Y, Iwatsuka H, et al. Reduction of insulin resistance in obese and/or diabetic animals by 5-[4-(1-methylcyclohexylmethoxy)benzyl]-thiazolidine-2,4-dione (ADD-3878, U-63,287, ciglitazone), a new antidiabetic agent. Diabetes. 1983;32(9): 804-10.

3. Lehmann JM, Moore LB, Smith-Oliver TA, Wilkison WO, Willson TM, Kliewer SA. An antidiabetic thiazolidinedione is a high affinity ligand for peroxisome proliferator-activated receptor gamma (PPAR gamma). The Journal of biological chemistry. 1995;270(22):12953-6.

4. Gallastegui N, Mackinnon JA, Fletterick RJ, Estebanez-Perpina E. Advances in our structural understanding of orphan nuclear receptors. Trends Biochem Sci. 2015;40(1): 25-35.

5. Kroker AJ, Bruning JB. Review of the structural and dynamic mechanisms of PPARγ partial agonism. PPAR Res. 2015;816856:1-15.

6. Edman K, Hosseini A, Bjursell MK, Aagaard A, Wissler L, Gunnarsson A, et al. Ligand Binding Mechanism in Steroid Receptors: From Conserved Plasticity to Differential Evolutionary Constraints. Structure. 2015;23(12):2280-90.

7. Aci-Seche S, Genest M, Garnier N. Ligand entry pathways in the ligand binding domain of PPARgamma receptor. FEBS letters. 2011;585(16):2599-603.

8. Genest D, Garnier N, Arrault A, Marot C, Morin-Allory L, Genest M. Ligand-escape pathways from the ligand-binding domain of PPARgamma receptor as probed by molecular dynamics simulations. Eur Biophys J. 2008;37(4):369-79.

9. Nolte RT, Wisely GB, Westin S, Cobb JE, Lambert MH, Kurokawa R, et al. Ligand binding and co-activator assembly of the peroxisome proliferator-activated receptor-gamma. Nature. 1998;395(6698):137-43.

10. Kim YG, Lou AC, Saghatelian A. A metabolomics strategy for detecting protein-metabolite interactions to identify natural nuclear receptor ligands. Mol Biosyst. 2011;7(4):1046-9.

11. Itoh T, Fairall L, Amin K, Inaba Y, Szanto A, Balint BL, et al. Structural basis for the activation of PPARgamma by oxidized fatty acids. Nat Struct Mol Biol. 2008.

12. Li Y, Zhang J, Schopfer FJ, Martynowski D, Garcia-Barrio MT, Kovach A, et al. Molecular recognition of nitrated fatty acids by PPAR gamma. Nat Struct Mol Biol. 2008;15(8): 865-7.

13. Waku T, Shiraki T, Oyama T, Fujimoto Y, Maebara K, Kamiya N, et al. Structural insight into PPARgamma activation through covalent modification with endogenous fatty acids. J Mol Biol. 2009;385(1):188-99.

14. Waku T, Shiraki T, Oyama T, Morikawa K. Atomic structure of mutant PPARgamma LBD complexed with 15d-PGJ2: novel modulation mechanism of PPARgamma/RXRalpha function by covalently bound ligands. FEBS letters. 2009;583(2):320-4.

15. Malapaka RR, Khoo S, Zhang J, Choi JH, Zhou XE, Xu Y, et al. Identification and mechanism of 10-carbon fatty acid as modulating ligand of peroxisome proliferator-activated receptors. The Journal of biological chemistry. 2012;287(1): 183-95.

16. Kliewer SA, Sundseth SS, Jones SA, Brown PJ, Wisely GB, Koble CS, et al. Fatty acids and eicosanoids regulate gene expression through direct interactions with peroxisome proliferator-activated receptors alpha and gamma. Proc Natl Acad Sci U S A. 1997;94(9):4318-23.

17. Ziouzenkova O, Perrey S, Asatryan L, Hwang J, MacNaul KL, Moller DE, et al. Lipolysis of triglyceride-rich lipoproteins generates PPAR ligands: evidence for an antiinflammatory role for lipoprotein lipase. Proc Natl Acad Sci U S A. 2003;100(5):2730-5.

18. Xu HE, Lambert MH, Montana VG, Parks DJ, Blanchard SG, Brown PJ, et al. Molecular recognition of fatty acids by peroxisome proliferator-activated receptors. Mol Cell. 1999;3(3):397-403.

19. Nagy L, Tontonoz P, Alvarez JG, Chen H, Evans RM. Oxidized LDL regulates macrophage gene expression through ligand activation of PPARgamma. Cell. 1998;93(2):229-40.

20. Hughes TS, Shang J, Brust R, de Vera IM, Fuhrmann J, Ruiz C, et al. Probing the Complex Binding Modes of the PPARgamma Partial Agonist 2-Chloro-N-(3-chloro-4-((5-chlorobenzo[d]thiazol-2-yl)thio)phenyl)-4-(trifluorome thyl)benzenesulfonamide (T2384) to Orthosteric and Allosteric Sites with NMR Spectroscopy. J Med Chem. 2016;59(22):10335-41.

21. Li Y, Wang Z, Furukawa N, Escaron P, Weiszmann J, Lee G, et al. T2384, a novel antidiabetic agent with unique peroxisome proliferator-activated receptor gamma binding properties. The Journal of biological chemistry. 2008;283(14): 9168-76.

22. Hughes TS, Giri PK, de Vera IM, Marciano DP, Kuruvilla DS, Shin Y, et al. An alternate binding site for PPARγ ligands. Nature communications. 2014;5:3571.

23. Brust R, Lin H, Fuhrmann J, Asteian A, Kamenecka TM, Kojetin DJ. Modification of the Orthosteric PPARgamma Covalent Antagonist Scaffold Yields an Improved Dual-Site Allosteric Inhibitor. ACS Chem Biol. 2017;12(4):969-78.

24. Jang JY, Koh M, Bae H, An DR, Im HN, Kim HS, et al. Structural basis for differential activities of enantiomeric PPARgamma agonists: Binding of S35 to the alternate site. Biochim Biophys Acta. 2017;1865(6):674-81.

25. Bae H, Jang JY, Choi CS-S, Lee J-J, Kim H, Jo A, et al. Mechanistic elucidation guided by covalent inhibitors for the development of anti-diabetic PPARγ ligands. Chem Sci. 2016;7:5523-9.

26. Choi JH, Banks AS, Estall JL, Kajimura S, Bostrom P, Laznik D, et al. Anti-diabetic drugs inhibit obesity-linked phosphorylation of PPARgamma by Cdk5. Nature. 2010;466(7305):451-6.

27. Choi JH, Banks AS, Kamenecka TM, Busby SA, Chalmers MJ, Kumar N, et al. Antidiabetic actions of a non-agonist PPARgamma ligand blocking Cdk5-mediated phosphorylation. Nature. 2011;477(7365):477-81.

28. Choi SS, Kim ES, Koh M, Lee SJ, Lim D, Yang YR, et al. A novel non-agonist peroxisome proliferator-activated receptor gamma (PPARgamma) ligand UHC1 blocks PPARgamma phosphorylation by cyclin-dependent kinase 5 (CDK5) and improves insulin sensitivity. The Journal of biological chemistry. 2014;289(38):26618-29.

29. Dietz M, Mohr P, Kuhn B, Maerki HP, Hartman P, Ruf A, et al. Comparative molecular profiling of the PPARalpha/gamma activator aleglitazar: PPAR selectivity, activity and interaction with cofactors. ChemMedChem. 2012;7(6): 1101-11.

30. Furnsinn C, Brunmair B, Meyer M, Neschen S, Furtmuller R, Roden M, et al. Chronic and acute effects of thiazolidinediones BM13.1258 and BM15.2054 on rat skeletal muscle glucose metabolism. Br J Pharmacol. 1999;128(6):1141-8.

31. Rial SA, Karelis AD, Bergeron KF, Mounier C. Gut Microbiota and Metabolic Health: The Potential Beneficial Effects of a Medium Chain Triglyceride Diet in Obese Individuals. Nutrients. 2016;8(5).

32. Liberato MV, Nascimento AS, Ayers SD, Lin JZ, Cvoro A, Silveira RL, et al. Medium chain fatty acids are selective peroxisome proliferator activated receptor (PPAR) gamma activators and pan-PPAR partial agonists. PloS one. 2012;7(5):e36297.

33. Nagao K, Yanagita T. Medium-chain fatty acids: functional lipids for the prevention and treatment of the metabolic syndrome. Pharmacol Res. 2010;61(3):208-12.

34. Kabsch W, Sander C. Dictionary of protein secondary structure: pattern recognition of hydrogen-bonded and geometrical features. Biopolymers. 1983;22(12):2577-637.

35. Gampe RT, Jr., Montana VG, Lambert MH, Miller AB, Bledsoe RK, Milburn MV, et al. Asymmetry in the PPARgamma/RXRalpha crystal structure reveals the molecular basis of heterodimerization among nuclear receptors. Mol Cell. 2000;5(3):545-55.

36. Bruning JB, Chalmers MJ, Prasad S, Busby SA, Kamenecka TM, He Y, et al. Partial agonists activate PPARgamma using a helix 12 independent mechanism. Structure. 2007;15(10):1258-71.

37. Amato AA, Rajagopalan S, Lin JZ, Carvalho BM, Figueira AC, Lu J, et al. GQ-16, a novel peroxisome proliferator-activated receptor gamma (PPARgamma) ligand, promotes insulin sensitization without weight gain. The Journal of biological chemistry. 2012;287(33):28169-79.

38. Tao H, Bausch C, Richmond C, Blattner FR, Conway T. Functional genomics: expression analysis of Escherichia coli growing on minimal and rich media. J Bacteriol. 1999;181(20):6425-40.

39. Hughes TS, Chalmers MJ, Novick S, Kuruvilla DS, Chang MR, Kamenecka TM, et al. Ligand and receptor dynamics contribute to the mechanism of graded PPARγ agonism. Structure. 2012;20(1):139-50.

40. Puhl AC, Bernardes A, Silveira RL, Yuan J, Campos JL, Saidemberg DM, et al. Mode of Peroxisome Proliferator-Activated Receptor gamma Activation by Luteolin. Molecular pharmacology. 2012;81(6):788-99.

41. Waku T, Shiraki T, Oyama T, Maebara K, Nakamori R, Morikawa K. The nuclear receptor PPARgamma individually responds to serotonin- and fatty acid-metabolites. The EMBO journal. 2010;29(19):3395-407.

42. Leesnitzer LM, Parks DJ, Bledsoe RK, Cobb JE, Collins JL, Consler TG, et al. Functional consequences of cysteine modification in the ligand binding sites of peroxisome proliferator activated receptors by GW9662. Biochemistry. 2002;41(21):6640-50.

43. Marciano DP, Kuruvilla DS, Boregowda SV, Asteian A, Hughes TS, Garcia-Ordonez R, et al. Pharmacological repression of PPARgamma promotes osteogenesis. Nature communications. 2015;6:7443.

44. Palusiak M, Grabowski SJ. Methoxy group as an acceptor of proton in hydrogen bonds. J Mol Struct. 2002;642(1-3):97-104.

45. Scheepstra M, Leysen S, van Almen GC, Miller JR, Piesvaux J, Kutilek V, et al. Identification of an allosteric binding site for RORgammat inhibition. Nature communications. 2015;6:8833.

46. Delfosse V, Dendele B, Huet T, Grimaldi M, Boulahtouf A, Gerbal-Chaloin S, et al. Synergistic activation of human pregnane X receptor by binary cocktails of pharmaceutical and environmental compounds. Nature communications. 2015;6:8089.

47. Chandra V, Huang P, Hamuro Y, Raghuram S, Wang Y, Burris TP, et al. Structure of the intact PPAR-gamma-RXR-nuclear receptor complex on DNA. Nature. 2008;456(7220):350-6.

48. Forman BM, Chen J, Evans RM. Hypolipidemic drugs, polyunsaturated fatty acids, and eicosanoids are ligands for peroxisome proliferator-activated receptors alpha and delta. Proc Natl Acad Sci U S A. 1997;94(9):4312-7.

49. Hostetler HA, Kier AB, Schroeder F. Very-long-chain and branched-chain fatty acyl-CoAs are high affinity ligands for the peroxisome proliferator-activated receptor alpha (PPARalpha). Biochemistry. 2006;45(24):7669-81.

50. Oswal DP, Balanarasimha M, Loyer JK, Bedi S, Soman FL, Rider SD, Jr., et al. Divergence between human and murine peroxisome proliferator-activated receptor alpha ligand specificities. J Lipid Res. 2013;54(9):2354-65.

51. Egawa D, Itoh T, Akiyama Y, Saito T, Yamamoto K. 17-OxoDHA Is a PPARalpha/gamma Dual Covalent Modifier and Agonist. ACS Chem Biol. 2016;11(9):2447-55.

52. Fyffe SA, Alphey MS, Buetow L, Smith TK, Ferguson MA, Sorensen MD, et al. Recombinant human PPAR-beta/delta ligand-binding domain is locked in an activated conformation by endogenous fatty acids. J Mol Biol. 2006;356(4):1005-13.

53. Bourguet W, Vivat V, Wurtz JM, Chambon P, Gronemeyer H, Moras D. Crystal structure of a heterodimeric complex of RAR and RXR ligand-binding domains. Mol Cell. 2000;5(2):289-98.

54. Egea PF, Mitschler A, Moras D. Molecular recognition of agonist ligands by RXRs. Mol Endocrinol. 2002;16(5):987-97.

55. Lengqvist J, Mata De Urquiza A, Bergman AC, Willson TM, Sjovall J, Perlmann T, et al. Polyunsaturated fatty acids including docosahexaenoic and arachidonic acid bind to the retinoid X receptor alpha ligand-binding domain. Mol Cell Proteomics. 2004;3(7):692-703.

56. Xu RX, Lambert MH, Wisely BB, Warren EN, Weinert EE, Waitt GM, et al. A structural basis for constitutive activity in the human CAR/RXRalpha heterodimer. Mol Cell. 2004;16(6):919-28.

57. Levi L, Wang Z, Doud MK, Hazen SL, Noy N. Saturated fatty acids regulate retinoic acid signalling and suppress tumorigenesis by targeting fatty acid-binding protein 5. Nature communications. 2015;6:8794.

58. Pawar A, Xu J, Jerks E, Mangelsdorf DJ, Jump DB. Fatty acid regulation of liver X receptors (LXR) and peroxisome proliferator-activated receptor alpha (PPARalpha) in HEK293 cells. The Journal of biological chemistry. 2002;277(42):39243-50.

59. Caputo M, De Rosa MC, Rescigno T, Zirpoli H, Vassallo A, De Tommasi N, et al. Binding of polyunsaturated fatty acids to LXRalpha and modulation of SREBP-1 interaction with a specific SCD1 promoter element. Cell Biochem Funct. 2014;32(8):637-46.

60. Bedi S, Hines GV, Lozada-Fernandez VV, de Jesus Piva C, Kaliappan A, Rider SD, Jr., et al. Fatty acid binding profile of the liver X receptor alpha. J Lipid Res. 2017;58(2):393-402.

61. Ducheix S, Montagner A, Polizzi A, Lasserre F, Regnier M, Marmugi A, et al. Dietary oleic acid regulates hepatic lipogenesis through a liver X receptor-dependent signaling. PloS one. 2017;12(7):e0181393.

62. Zhao A, Yu J, Lew JL, Huang L, Wright SD, Cui J. Polyunsaturated fatty acids are FXR ligands and differentially regulate expression of FXR targets. DNA Cell Biol. 2004;23(8):519-26.

63. Mitsuhashi N, Mizuno M, Miyagawa A, Kato J. Inhibitory effect of fatty acids on the binding of androgen receptor and R1881. Endocrinol Jpn. 1988;35(1):93-6.

64. Inoue A, Yamamoto N, Morisawa Y, Uchimoto T, Yukioka M, Morisawa S. Unesterified long-chain fatty acids inhibit thyroid hormone binding to the nuclear receptor. Solubilized receptor and the receptor in cultured cells. Eur J Biochem. 1989;183(3):565-72.

65. van der Klis FR, Schmidt ED, van Beeren HC, Wiersinga WM. Competitive inhibition of T3 binding to alpha 1 and beta 1 thyroid hormone receptors by fatty acids. Biochem Biophys Res Commun. 1991;179(2):1011-6.

66. Menendez JA, Colomer R, Lupu R. Omega-6 polyunsaturated fatty acid gamma-linolenic acid (18:3n-6) is a selective estrogen-response modulator in human breast cancer cells: gamma-linolenic acid antagonizes estrogen receptor-dependent transcriptional activity, transcriptionally represses estrogen receptor expression and synergistically enhances tamoxifen and ICI 182,780 (Faslodex) efficacy in human breast cancer cells. Int J Cancer. 2004;109(6):949-54.

67. Moutsatsou P, Papoutsi Z, Kassi E, Heldring N, Zhao C, Tsiapara A, et al. Fatty acids derived from royal jelly are modulators of estrogen receptor functions. PloS one. 2010;5(12):e15594.

68. Kato J, Takano A, Mitsuhashi N, Koike N, Yoshida K, Hirata S. Modulation of brain progestin and glucocorticoid receptors by unsaturated fatty acid and phospholipid. J Steroid Biochem. 1987;27(4-6):641-8.

69. Viscardi RM, Max SR. Unsaturated fatty acid modulation of glucocorticoid receptor binding in L2 cells. Steroids. 1993;58(8):357-61.

70. Vallette G, Vanet A, Sumida C, Nunez EA. Modulatory effects of unsaturated fatty acids on the binding of glucocorticoids to rat liver glucocorticoid receptors. Endocrinology. 1991;129(3):1363-9.

71. Dhe-Paganon S, Duda K, Iwamoto M, Chi YI, Shoelson SE. Crystal structure of the HNF4 alpha ligand binding domain in complex with endogenous fatty acid ligand. The Journal of biological chemistry. 2002;277(41):37973-6.

72. Wisely GB, Miller AB, Davis RG, Thornquest AD, Jr., Johnson R, Spitzer T, et al. Hepatocyte nuclear factor 4 is a transcription factor that constitutively binds fatty acids. Structure. 2002;10(9):1225-34.

73. de Vera IM, Giri PK, Munoz-Tello P, Brust R, Fuhrmann J, Matta-Camacho E, et al. Identification of a Binding Site for Unsaturated Fatty Acids in the Orphan Nuclear Receptor Nurr1. ACS Chem Biol. 2016;11(7):1795-9.

74. de Vera IMS, Munoz-Tello P, Dharmarajan V, Marciano DP, Matta-Camacho E, Giri PK, et al. Defining a canonical ligand-binding pocket in the orphan nuclear receptor Nurr1. bioRxiv. 2018:https://doi.org/10.1101/278440.

75. Vinayavekhin N, Saghatelian A. Discovery of a protein-metabolite interaction between unsaturated fatty acids and the nuclear receptor Nur77 using a metabolomics approach. J Am Chem Soc. 2011;133(43):17168-71.

76. Xie S, Lee YF, Kim E, Chen LM, Ni J, Fang LY, et al. TR4 nuclear receptor functions as a fatty acid sensor to modulate CD36 expression and foam cell formation. Proc Natl Acad Sci U S A. 2009;106(32):13353-8.

77. Sumida C. Fatty acids: ancestral ligands and modern co-regulators of the steroid hormone receptor cell signalling pathway. Prostaglandins Leukot Essent Fatty Acids. 1995;52(2-3):137-44.

78. McPhail LC, Clayton CC, Snyderman R. A potential second messenger role for unsaturated fatty acids: activation of Ca2+-dependent protein kinase. Science. 1984;224(4649): 622-5.

79. Murakami K, Routtenberg A. Direct activation of purified protein kinase C by unsaturated fatty acids (oleate and arachidonate) in the absence of phospholipids and Ca2+. FEBS letters. 1985;192(2):189-93.

80. Khan WA, Blobe GC, Hannun YA. Arachidonic acid and free fatty acids as second messengers and the role of protein kinase C. Cell Signal. 1995;7(3):171-84.

81. Stoddart LA, Smith NJ, Milligan G. International Union of Pharmacology. LXXI. Free fatty acid receptors FFA1, -2, and -3: pharmacology and pathophysiological functions. Pharmacol Rev. 2008;60(4):405-17.

82. Yonezawa T, Kurata R, Yoshida K, Murayama MA, Cui X, Hasegawa A. Free fatty acids-sensing G protein-coupled receptors in drug targeting and therapeutics. Curr Med Chem. 2013;20(31):3855-71.

83. Ordway RW, Singer JJ, Walsh JV, Jr. Direct regulation of ion channels by fatty acids. Trends Neurosci. 1991;14(3):96-100.

84. Antollini SS, Barrantes FJ. Fatty Acid Regulation of Voltage- and Ligand-Gated Ion Channel Function. Front Physiol. 2016;7:573.

85. Lindsley JE, Rutter J. Whence cometh the allosterome? Proc Natl Acad Sci U S A. 2006;103(28):10533-5.

86. Gallego O, Betts MJ, Gvozdenovic-Jeremic J, Maeda K, Matetzki C, Aguilar-Gurrieri C, et al. A systematic screen for protein-lipid interactions in Saccharomyces cerevisiae. Mol Syst Biol. 2010;6:430.

87. Li X, Gianoulis TA, Yip KY, Gerstein M, Snyder M. Extensive in vivo metabolite-protein interactions revealed by large-scale systematic analyses. Cell. 2010;143(4):639-50.

88. Li X, Snyder M. Metabolites as global regulators: a new view of protein regulation: systematic investigation of metabolite-protein interactions may help bridge the gap between genome-wide association studies and small molecule screening studies. Bioessays. 2011;33(7):485-9.

89. Orsak T, Smith TL, Eckert D, Lindsley JE, Borges CR, Rutter J. Revealing the allosterome: systematic identification of metabolite-protein interactions. Biochemistry. 2012;51(1):225-32.

90. Link H, Kochanowski K, Sauer U. Systematic identification of allosteric protein-metabolite interactions that control enzyme activity in vivo. Nat Biotechnol. 2013;31(4):357-61.

91. Bligh EG, Dyer WJ. A rapid method of total lipid extraction and purification. Can J Biochem Physiol. 1959;37(8): 911-7.

92. Armstrong EH, Goswami D, Griffin PR, Noy N, Ortlund EA. Structural basis for ligand regulation of the fatty acid-binding protein 5, peroxisome proliferator-activated receptor beta/delta (FABP5-PPARbeta/delta) signaling pathway. The Journal of biological chemistry. 2014;289(21):14941-54.

93. Battye TG, Kontogiannis L, Johnson O, Powell HR, Leslie AG. iMOSFLM: a new graphical interface for diffraction-image processing with MOSFLM. Acta crystallographica Section D, Biological crystallography. 2011;67(Pt 4):271-81.

94. Winn MD, Ballard CC, Cowtan KD, Dodson EJ, Emsley P, Evans PR, et al. Overview of the CCP4 suite and current developments. Acta crystallographica Section D, Biological crystallography. 2011;67(Pt 4):235-42.

95. McCoy AJ, Grosse-Kunstleve RW, Adams PD, Winn MD, Storoni LC, Read RJ. Phaser crystallographic software. Journal of applied crystallography. 2007;40(Pt 4):658-74.

96. Adams PD, Afonine PV, Bunkoczi G, Chen VB, Davis IW, Echols N, et al. PHENIX: a comprehensive Python-based system for macromolecular structure solution. Acta crystallographica Section D, Biological crystallography. 2010;66(Pt 2): 213-21.

97. Emsley P, Cowtan K. Coot: model-building tools for molecular graphics. Acta crystallographica Section D, Biological crystallography. 2004;60(Pt 12 Pt 1):2126-32.

98. Ho BK, Gruswitz F. HOLLOW: generating accurate representations of channel and interior surfaces in molecular structures. BMC Struct Biol. 2008;8:49.

99. Johnson BA. Using NMRView to visualize and analyze the NMR spectra of macromolecules. Methods Mol Biol. 2004;278:313-52.

100. Williamson MP. Using chemical shift perturbation to characterise ligand binding. Progress in nuclear magnetic resonance spectroscopy. 2013;73:1-16.

101. Giaginis C, Theocharis S, Tsantili-Kakoulidou A. A consideration of PPAR-gamma ligands with respect to lipophilicity: current trends and perspectives. Expert Opin Investig Drugs. 2007;16(4):413-7.

102. Pettersen EF, Goddard TD, Huang CC, Couch GS, Greenblatt DM, Meng EC, et al. UCSF Chimera--a visualization system for exploratory research and analysis. Journal of computational chemistry. 2004;25(13):1605-12.

103. Dupradeau FY, Pigache A, Zaffran T, Savineau C, Lelong R, Grivel N, et al. The R.E.D. tools: advances in RESP and ESP charge derivation and force field library building. Phys Chem Chem Phys. 2010;12(28):7821-39.

104. Sali A, Blundell TL. Comparative protein modelling by satisfaction of spatial restraints. J Mol Biol. 1993;234(3): 779-815.

105. Anandakrishnan R, Aguilar B, Onufriev AV. H++ 3.0: automating pK prediction and the preparation of biomolecular structures for atomistic molecular modeling and simulations. Nucleic Acids Res. 2012;40(Web Server issue):W537-41.

106. Joung IS, Cheatham TE, 3rd. Molecular dynamics simulations of the dynamic and energetic properties of alkali and halide ions using water-model-specific ion parameters. J Phys Chem B. 2009;113(40):13279-90.

107. Jorgensen WL, Chandrasekhar J, Madura JD, Impey RW, Klein ML. Comparison of simple potential functions for simulating liquid water. J Chem Phys. 1983;79(2):926-35.

108. Maier JA, Martinez C, Kasavajhala K, Wickstrom L, Hauser KE, Simmerling C. ff14SB: Improving the Accuracy of Protein Side Chain and Backbone Parameters from ff99SB. J Chem Theory Comput. 2015;11(8):3696-713.

109. Hopkins CW, Le Grand S, Walker RC, Roitberg AE. Long-Time-Step Molecular Dynamics through Hydrogen Mass Repartitioning. J Chem Theory Comput. 2015;11(4):1864-74.

110. Ryckaert JP, Ciccotti G, Berendsen HJC. Numerical integration of the cartesian equations of motion of a system with constraints: molecular dynamics of n-alkanes. J Comput Phys. 1977;23(3):327-41.

111. Roe DR, Cheatham TEI. PTRAJ and CPPTRAJ: Software for Processing and Analysis of Molecular Dynamics Trajectory Data. J Chem Theory Comput. 2013;9(7):3084-95.

112. Fabiola F, Bertram R, Korostelev A, Chapman MS. An improved hydrogen bond potential: impact on medium resolution protein structures. Protein Sci. 2002;11(6):1415-23.

113. Perdew JP, Burke K, Ernzerhof M. Generalized gradient approximation made simple. Phys Rev Lett. 1996;77(18):3865-8.

114. Parr R, Yang W. Density-Functional Theory of Atoms and Molecules Oxford Univ. Press, New York. 1989.

115. Keller S, Vargas C, Zhao H, Piszczek G, Brautigam CA, Schuck P. High-precision isothermal titration calorimetry with automated peak-shape analysis. Anal Chem. 2012;84(11):5066-73.

116. Zhao H, Piszczek G, Schuck P. SEDPHAT--a platform for global ITC analysis and global multi-method analysis of molecular interactions. Methods. 2015;76:137-48.

117. Brautigam CA, Zhao H, Vargas C, Keller S, Schuck P. Integration and global analysis of isothermal titration calorimetry data for studying macromolecular interactions. Nat Protoc. 2016;11(5):882-94.

118. Brautigam CA. Calculations and Publication-Quality Illustrations for Analytical Ultracentrifugation Data. Methods Enzymol. 2015;562:109-33.